Master-Thesis

Montanuniversität Leoben
Department of Materials Physics

Thermo-mechanical behaviour of Mo-Ag thin films

Author:
Claus O. W. Trost

September 2018

AFFIDAVIT

I declare in lieu of oath, that I wrote this thesis and performed the associated research myself, using only literature cited in this volume.

Leoben, September 2018 Claus O. W. Trost

> “However, I continue to try and I continue, indefatigably, to reach out. There’s no way I can single-handedly save the world or, perhaps, even make a perceptible difference - but how ashamed I would be to let a day pass without making one more effort.”
>
> **— Isaac Asimov**

Abstract

In this work, the thermo-mechanical behaviour, the evolution of phases of thin films consisting of the immiscible system Molybdenum-Silver (Mo-Ag) were investigated. The 40 nm to 770 nm thick films were deposited via a dc magnetron sputtering process on rigid (Silicon) and flexible (Polyimide) substrates. The compositions ranged from 9 at.% to pure silver films, with a focus on the Mo-rich films. It was observed that differences in terms of composition and film thickness in the rigid system led to differences in thermo-mechanical behaviour. These differences were evaluated using different annealing treatments in a wafer curvature system and then they were used to interpret the behaviour of the flexible counterparts. Via X-Ray diffraction it was observed that phases ranged from metastable phases before annealing and after annealing to segregated Mo-rich and Ag-rich phases. The surface evolution was found to evolve with increasing silver content and with both time and temperature.

Kurzfassung

In der vorliegenden Arbeit wurden das thermo-mechanische Verhalten und die daraus resultierenden Veränderungen der Phasen von metallischen dünnen Filmen des unmischbaren Systems Molybdän-Silber (Mo-Ag) untersucht. Die 40 nm bis 70 nm dicken Schichten wurden mittels eines DC-Magnetron-Sputter Prozesses auf biegesteifes (Silizium) und flexibles (Polyimid) Substrat aufgebracht. Die Zusammensetzungen erstreckten sich von 9 atm. % Ag bis zu reinen Silberfilmen. Es wurde festgestellt, dass die Zusammensetzungs- und Dickenvariationen zu Unterschieden im thermo-mechanischen Verhalten führten. Das thermo-mechanische Verhalten wurde mittels der Wafer-Krümmungs-Methode festgestellt und zur Interpretation des Verhaltens der flexiblen Proben verwendet. Die Phasenveränderungen wurden mittels Röntgenbeugung untersucht. Metastabile Phasen wurden vor der Wärmebehandlung festgestellt. Nach der Wärmebehandlung wurden durch Segregation entstandene Molybdän und Silber reiche Phasen entdeckt. Die Veränderung der Oberfläche ging, wie für einen diffusionskontrollierten Prozess üblich, Hand in Hand mit Zeit und Temperatur.

Contents

1 Introduction 7

2 Literature overview 8

2.1 Thin film deposition - Sputtering 8

2.2 X-ray Diffraction 10

2.2.1 Synchrotron radiation and its applications 12

2.2.2 Estimating crystallite sizes 14

2.2.2.1 Scherrer method 15

2.2.2.2 Williamson-Hall Analysis 16

2.3 Film stress measurements and thin film mechanics 18

2.3.1 Sin^{2}Ψ-Method 18

2.3.2 Wafer Curvature 21

3 Materials and Experiments 24

4 Results 28

4.1 Rigid Substrates 28

4.1.1 Film stress 29

4.1.1.1 Thermal stress evolution 29

4.1.1.2 Sin^{2}Ψ-Method 34

4.1.2 Surface Features after Annealing 35

4.2 Flexible Substrates 41

4.2.1 Crystallite size estimation 42

4.2.1.1 Mo crystallite size 42

4.2.1.2 Ag crystallite size 43

4.2.2 Film stress measurement 43

4.2.3 Surface features after annealing 44

5 Discussion 48

6 Conclusions and Outlook 51

7 Acknowledgements 52

List of figures 53

List of tables *55*

References *56*

1 Introduction

The thermo-mechanical behaviour of metallic films has been studied for more than four decades. In the last decade metallic films on flexible substrates have received increasing attention due to the potential of revolutionizing the functionality of electronic devices [1]. Prototypes that can be folded, rolled and bent have already been produced [2, 3]. The often brittle metal films, although frequently being responsible for the failure of the flexible microelectronic parts, can not easily be replaced due to other functional properties necessary to guarantee the performance of the devices [4–6]. Mo films are often chosen as a result of their combination of functional properties [4]. For example Mo thin films on Polyimide are used as back contacts for copper indium gallium diselenide and copper indium disufide, conductors because they are promising candidates to replaced bulk silicon in photovoltaic applications [7, 8]. Polyimides are used since they fulfil the basic requirements for usage as substrates such as high thermal stability, chemical inertness, low density, suitable coefficient of thermal expansion and low surface roughness [8]. Generally, using flexible substrates instead of glass substrates in photovoltaics would lead to significant weight loss and possibly enable roll-to-roll processes and decreasing fabrication costs [8].

Since sputtering enables production of a wide range of different material combinations, immiscible systems like Molybdenum-Silver (Mo-Ag) are candidates not only to improve mechanical stability, but also decrease resistivity. The system is well known for its so called “chameleon coatings” in combination with yttria-stabilized zirconia, coatings that automatically adapt their surface composition to minimize friction [9–11]. It has also been interest of research due to its tendency to build metastable phases and phase separations [12]. This combination of metastable phases and segregations on the surface could possibly lead to healing of cracks in flexible microelectronics as a diffusion controlled mechanism and thereby leading to longer lasting flexible microelectronic devices.

2 Literature overview

2.1 Thin film deposition - Sputtering

Film deposition can be classified by the different used physical, chemical or electrochemical mechanisms which are used to grow a film on a substrate. Most importantly there are physical vapour deposition (PVD), chemical vapour deposition (CVD) and electrochemical deposition. It is important to distinguish between the different classifications. According to [13] PVD processes (including evaporation and sputtering) and CVD processes can be distinguished by specific factors such as: The dependence of PVD on solid or molten sources [13]. Physical mechanisms that are used in PVD processes such as evaporation or impacts that provide atoms in their gas state and specific vacuum environment is needed to ensure transportation of material in gas state [13]. The non-appearance of chemical reactions both in the gas state and on the surface of the substrate are also typical for PVD, making reactive PVD processes exceptions [13].

In general sputtering is classified as a PVD process. Sputtering can be subdivided into four categories dc (direct current), RF (radio frequency), magnetron and reactive sputtering [13].The sputtering treatment takes place in a vacuum chamber, including one or more sputter targets and holders for the substrates. To ensure that no contamination of the deposited film by any other material happens, to counter scattering of the sputtered atoms by gases and to establish plasma vacuum is needed. Sputter targets consist of pure metals or alloys. They can be fabricated by melting under protective atmospheres or in vacuum, targets made out of refractory metals are usually produced via different powder metallurgy routes [13]. Substrates can be both, rigid or flexible, with a limiting factor would be that it has to be resistant to the vacuum conditions. After reaching a vacuum of about 10^{-2}-10^{-3} [14] (depending on the process), Argon gas is inserted into the camber. The gas is then ionized and forms a plasma state. The Argon plasma consist of Ar^+ Ions, they are used to eject the material from the target to deposit on the substrate. This is done by applying an electric field to the target and the sample. The Ar^+ Ions are accelerated towards the negative target or targets, causing neutral metal to be ejected and are then deposited on the substrate, as shown in Figure 1. To release the neutral metal atom, by transfer of the momentum, the binding energy needs to be exceeded by the kinetic energy of the impinging ion [15]. The film growth can be described by different models. Either it is proposed that the film grows as islands consisting of three-dimensional crystals that act as nuclei for growth (Volmer-Weber model) or as monolayer islands that grow together (Frank and Vander Merwe model) [16]. The Stransky and Krastanov model combines both discrete three-dimensional nucleation and the layer-by-layer growth [16]. For detailed description and other models see [16]. As a result of the film growth mechanisms material combinations are possible, which wouldn't be access able with other processing routes, such as intermetallics, solid solutions, or metallic glasses.

The production of nanocomposite films via sputtering in binary metal system can be described by several models. According to [17] the main parameters for controlling the film composition and structure are the type and the amount of the mixing elements. Also, the miscibility or immiscibility of the film elements, the ability to form solid solutions or intermetallic compounds and the enthalpy of alloy formation, ΔH_i, have to be taken into account [17]. Generally, it is proposed that binary metal films composed of A and B should create a polycrystalline structure if the elements form a solid solution (e.g. NiCr 80/20wt. % [18]) [17]. Additionally polycrystalline films should also be found if the elements do not form intermetallic compounds, are immiscible and the enthalpy of film formation ΔH_f is positive (e.g. ZrY 90/10 wt. % [19]). To achieve nanocrystalline or amorphous films A and B should be immiscible, have a negative ΔH_f and form many different intermetallic phases (e.g. ZrCu 70/30 wt.% [20]) [17].

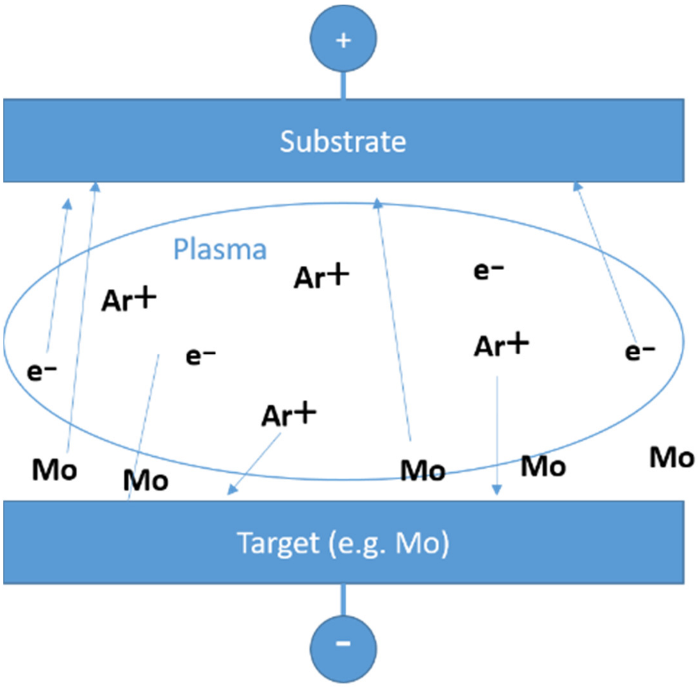

Figure 1: Schematic of a sputter process. The plasma consists of positively charged Ions and electrons. By applying negative charge to the target, the Ions begin to impinge on it and thereby causing neutral metal atoms to be ejected. The neutral metal atoms can move through the plasma and begin to form a metallic film on the substrate.

2.2 X-ray Diffraction

When a polycrystalline material is exposed to a monochromatic X-ray beam diffraction takes place. This arises classically seen due to the Huygens-Fresnel principle as seen in Figure 2. Generally speaking, diffraction occurs only when the wave encounters obstacles such as slits with approximately the distance as the wavelength of the incident beam. It is a product of both constructive and destructive interference of the newly produced waves.

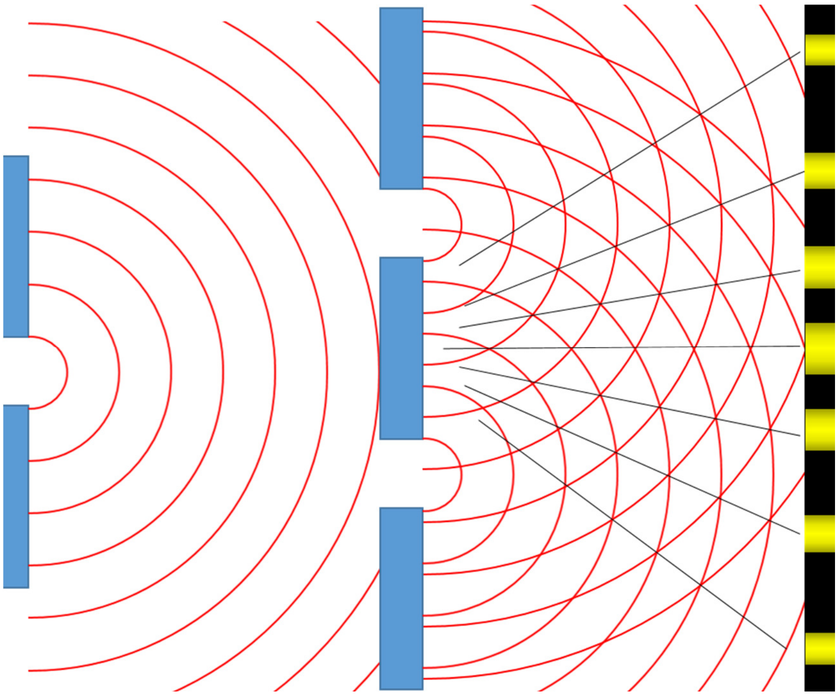

Figure 2: Schematic of a double slit-experiment showing Huygens-Fresnel principle and the production of a simple diffraction pattern. The yellow areas symbolize maxima and the black areas minima of the pattern.

Since the wavelength of X-Rays (e.g. 1.5406 Å for CuK_{α}) and the shortest interatomic distances of crystals (~0.5 Å to ~2.5 Å) are in the same dimension diffraction is obtainable [21, 22]. Note that it is important that X-rays are not scattered by the nuclei but from the electrons, more accurately they are scattered by the electron density which is distributed periodically in the crystal lattice [22]. Generated diffraction patterns are then collected by a suitable detector. The patterns are called Debye Scherrer rings, a typical ring and the experimental setup is shown in Figure 3.

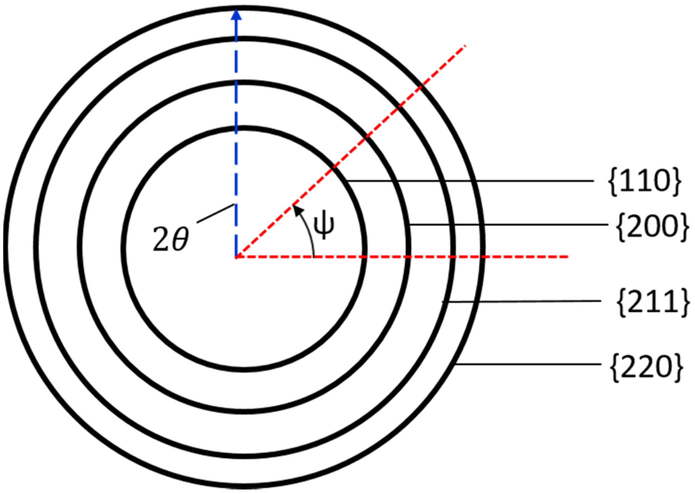

Figure 3: Schematic of ideal Debye Scherrer rings for a base centred cubic system (bcc). The corresponding crystallographic planes and angles are indicated.

In a pure polycrystalline metal, each ring in the pattern corresponds to one specific crystallographic plane. Depending on the crystalline structure of the material there are both allowed and forbidden reflections, therefore, not every plane will cause a ring to form. This is described by the structure factor, defined by formula 2.1, for a detailed derivation see [23]

$$S_G(hkl) = \sum_j f_j \exp[-i2\pi(hx_j + ky_j + lz_j)], \qquad (2.1)$$

where S_G is the structure factor, f_j represents the scattering factor of the atom number j. The symbols, h, k, l are the Miller indices and x, y, z are the fractional coordinates of the atoms.

To calculate the structure factor we need to know where the atoms are placed in the cell.

For face centred cubic (fcc):

fcc consists of 4 Atoms placed on $0/0/0$, $\frac{1}{2}/\frac{1}{2}/0$, $\frac{1}{2}/0/\frac{1}{2}$ and $0/\frac{1}{2}/\frac{1}{2}$.

$$S = 4f \text{ if h, k, l are all odd or all even numbers}$$

$$S = 0\ if\ h, k, l\ are\ mixed$$

So the planes like (111), (200), (220) will produce reflection but the reflections of (100), (221) are forbidden.

The same approach can be applied to all other systems leading to:

$$S = 2f \text{ if } \mathrm{h + k + l} \text{ equals an even number}$$

$$S = 0 \text{ if } \mathrm{h + k + l} \text{ equals an odd number}$$

for base centred cubic systems (bcc).

Not only the structure of the material can be defined by the ring pattern, also other factors such as composition, texture, stress and crystallite-sizes have an influence on the pattern [24]. For example a preferred texture would shift the distribution of the bright spots on the rings from evenly distributed to certain areas with higher brightness and others without.

To be able to differentiate easily between different phases, or in general to see the composition and get a value for the crystallite size, the whole ring pattern is integrated over the azimuthal angle. The calculated curves are called *θ-2θ* plots. A typical plot is shown in Figure 4. By plotting the Intensity over the θ angles the peaks are easily comparable with literature data.

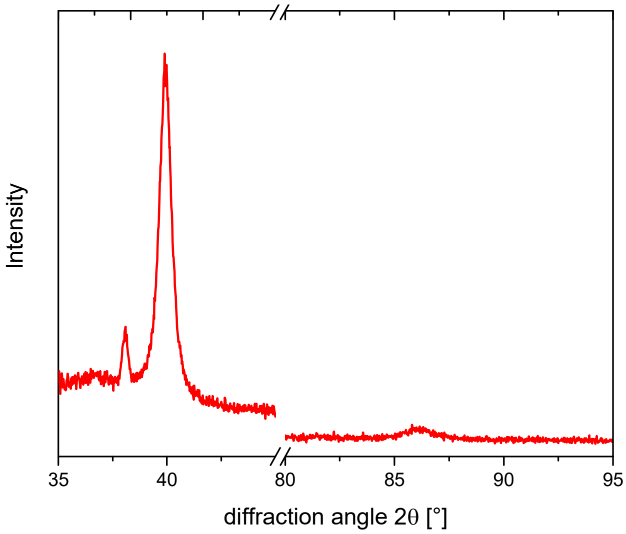

Figure 4: Significant parts of a θ-2θ scan of sputtered Mo-Ag on Polyimide with a thickness of 50 nm. The first small peak belongs to the Ag (111) plane, the second one to Mo (110) and the last one to Mo (222).

2.2.1 Synchrotron radiation and its applications

Synchrotrons are interdisciplinary used large scientific facilities. Scientists from the fields of materials science, biology, medicine, geology and chemistry use the high-brilliance beams, produced by the third-generation synchrotron radiation (SR) sources, to produce cutting edge scientific research [25]. A synchrotron basically accelerates charged particles such as electrons to enormous energies [26]. The produced electron beam travels close to the speed of light [26]. To achieve this, strong electric and magnetic fields are needed which have to be simultaneously increased in terms of strength [26].

At the early stages, synchrotrons were only used for particle physics applications, studying collisions between subatomic particles [26]. The first synchrotron light sources were even called parasitic as seen in Figure 5a, since they were built into existing synchrotrons [27]. To not interfere with particle physics the second generation sources where build as early as 1981 and they were dedicated to harness the synchrotron radiation (SR) [26, 27]. In 1994 the first third generation Synchrotron the European Synchrotron Radiation Facility (ESRF) in Grenoble was completed [27]. The third generation is optimising the intensity of the SR by so called insertion devices such as undulators and wigglers described by Figure 5 and Figure 6 [26]. Therefore, the sources have significant advantages to conventionally used X-Ray sources, they provide an extremely wide spectral range ranging from infrared to X-Rays, high polarization, natural collimation, high stability and pulsed time structure [25]. By combining these properties a never before known range of measurements is possible [25].

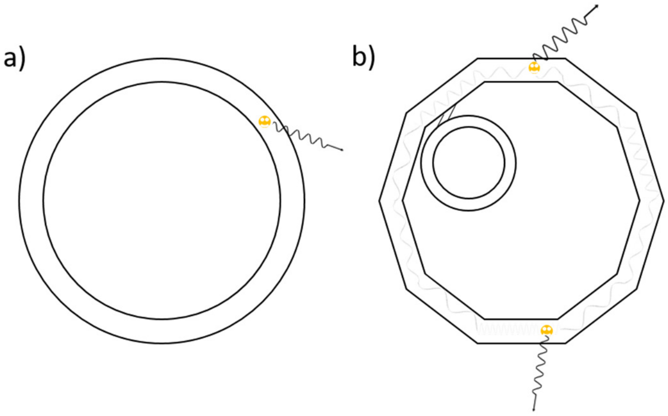

Figure 5: Schematic of two different synchrotron facilities. Smileys represent electrons and outgoing SR waves. a) An older synchrotron where the radiation is only generated by bending magnets through the circular motion of the electrons. b) A modern synchrotron consisting of a particle accelerator in the middle and a storage ring around it that mainly consists of straight sections which contain insertion devices like wigglers and undulators to produce SR. Figure analogous to [28].

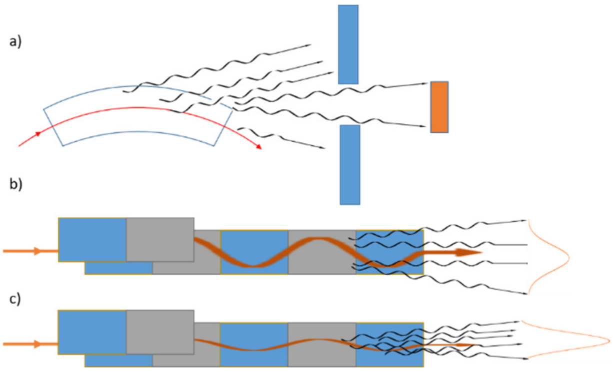

Figure 6: Schematics of different methods to produce SR. a) Bending magnet produces SR as a result of the circular motion of the electrons. b) Wiggler works like bending magnets, but has a higher magnetic field and therefore photons with higher energies are produced. c) Undulator produces highly peaked spectrum by a small source with shallow bends. Figure analogous to [29].

2.2.2 Estimating crystallite sizes

The difference between crystallite size and the commonly used term grain size is emphasised in Figure 7 and described in [30]. A grain can consist of various crystals that are bound together and are differentiated in a light microscope [30]. This is a result of high angle grain boundaries (HAGBs) being more pronounced through etching and are more visible in a light microscope.

With X-ray diffraction (XRD) methods it is normally not possible to measure the grain size. The crystal size is only obtainable by XRD if a single crystal is measured. Crystals consist of several crystallites, they are merged together by small angle grain boundaries (SAGBs) which are basically made up dislocations (for symmetrical SABGs one band of edge dislocations) [30, 31]. This means that they only have a slight orientation difference (misorientation <15°[31]), which might not be measureable with other techniques. Domains are the subdivisions of crystallites [30]. They are defined by two-dimensional defects, e.g. stacking faults and twin boundaries. Domains divided by such defects still have well defined relations regarding crystal lattice [30]. Diffraction depends on the relation of the diffracting crystal planes and its boundaries [30]. This is one limiting factor of XRD methods and to gain more information on domains and defects complementary methods such as high resolution transmission electron microscopy (HRTEM) should be used [30].

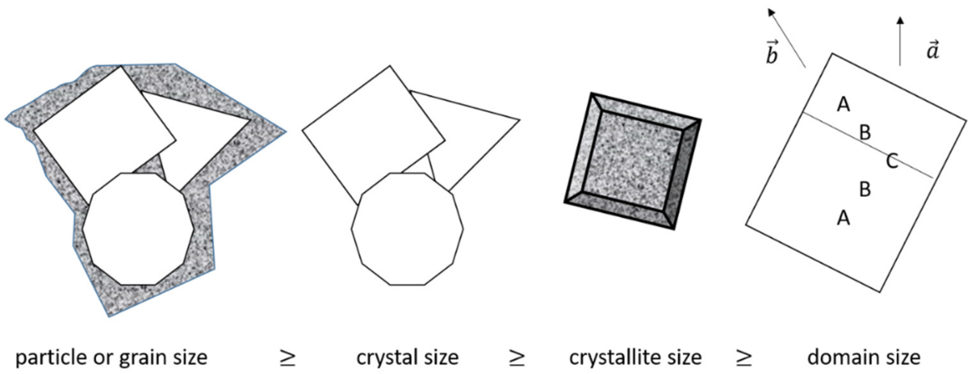

Figure 7: Schematic of different measurable sizes of a material (analogous to [30]).

2.2.2.1 Scherrer method

To estimate the crystallite size of the material the Scherrer Equation [32] can be used. Note that the symbols used today differ from the original used by Scherrer 1918 [30].

$$B(2\theta) = \frac{K * \lambda}{L * \cos(\theta)} \tag{2.2}$$

K is the constant of proportionality also called Scherrer constant, *L* is the crystallite size, λ corresponds to the wavelength of the radiation and $B(2\theta)$ to the peak width that can be calculated in various ways like the FWHM approach or the integral breadth as seen in Figure 8 [24]. The Scherrer constant varies from 0.62 to 2.08 and the chosen value depends on the method of width determination, shape of the crystal and the size distribution [24]. For example, if one uses a common cubic symmetry, spherical crystals determined by the full width half maximum (FWHM) [24] would suggest a value of 0.94. Most of the times 0.9 is a sufficient approximation [33]. For more information see [34], who tabulated values for *K* for various systems. Keep in mind that results can differ, if different assumptions were made and therefore different K values were chosen [30]. This has to be taken into account when one wants to compare the results of different calculation methods or when comparing with complimentary techniques such as transmission electron microscopy (TEM) [30].

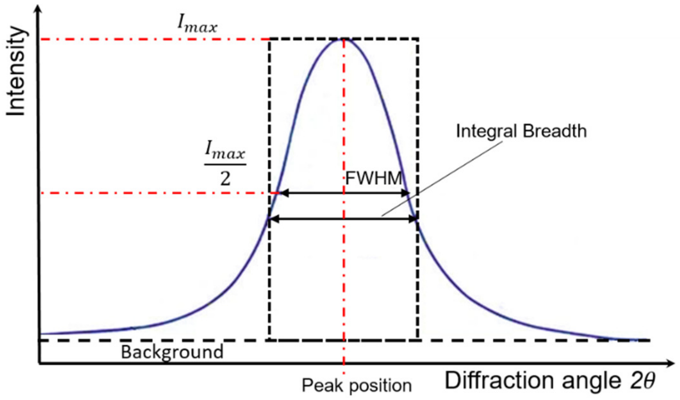

Figure 8: Full width at half maximum and integral breadth

The Equation 2.2 describes that the peak width varies with crystallite size. The larger the crystallite size, the smaller the peak width. Also the peak width depends on the θ-angle [24]. At large angles, the broadening of the crystallite size becomes more pronounced [24]. The problem with this is that at high θ-angles broadening also due to the instrumental profile width and microstrains is largest [24], making the peak intensity weaker at large θ-angles (Figure 4) [24]. As a result, if only one peak is used it is proposed by [24] to use peaks between the θ-angles of 30° and 50°, since below 30° peak asymmetry compromises the profile analysis [24].

Another problem with measuring the peak width is that the width can not only be attributed to crystallite size but also to various other effects such as instrumental peak broadening, microstrains, peak broadening as a result of solid solution inhomogeneities and temperature factors [24].

2.2.2.2 Williamson-Hall Analysis

The method was proposed by Williamson and Hall in 1953 [35] in order to refine the Scherrer equation and to implement crystal imperfections and distortions of micro-strain induced peak broadening. The term $\varepsilon \approx \beta_s / tan\theta$ is added to the broadening leading to equation 2.7 [22, 35–37]. The main difference to the classical Scherrer formula is that in the Williams Hall formula takes into account that both small crystallite size and microstrains occur together and change the peak broadening [36].

To ensure the quality of the data the instrumental broadening has to be taken into account. Instrumental peak broadening is measured using materials such as LaB_6, Al_20_3 or BaF_2 which theoretically should not exhibit measurable sample broadening [38]. Depending on the shape of the peak, examples can be seen in Figure 9, the β_{total} can be calculated with different approaches [39],

For Gaussian profiles [39]:

$$\beta_{total}^2 = (\beta_{measured}^2 - \beta_{instrumental}^2) \tag{2.3}$$

For Lorentzian profiles [39]:

$$\beta_{total} = (\beta_{measured} - \beta_{instrumental}) \tag{2.4}$$

In the absence of the exact nature of the peak, the geometric mean is used [39]:

$$\beta_{total} = \sqrt{(\beta_{measured} - \beta_{instrumental}) * \sqrt{(\beta_{measured}^2 - \beta_{instrumental}^2)}} \tag{2.5}$$

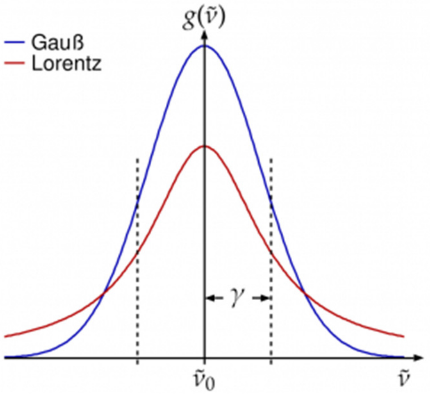

Figure 9: Comparison Gauss and Lorentz Profiles, taken with creative common license from [40].

To calculate the crystallite size take β_{total} and treat it as equal to the former described Scherrer equation and β_s.

$$\beta_{total} = \left(\frac{K\,\lambda}{\mathrm{L}\cos(\theta)}\right) + \beta_s \tag{2.6}$$

$$\beta_{total} = \left(\frac{K\,\lambda}{\mathrm{L}\cos(\theta)}\right) + 4\,\varepsilon\tan(\theta) \tag{2.7}$$

Rearranging leads to:

$$\beta_{total} * \cos(\theta) = 4\,\varepsilon\sin(\theta) + \left(\frac{K\,\lambda}{L}\right) \tag{2.8}$$

Where ε is the strain and β_D is the strain broadening [37].

Equation 2.8 resembles the formula of a straight line: $y = kx + d$. Therefore, the obtained data can be plotted as seen in Figure 10 and the crystallite size can be calculated.

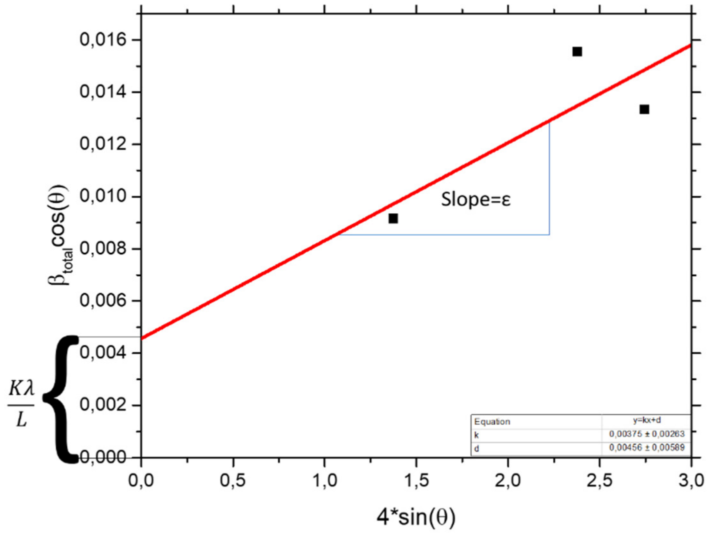

Figure 10: Williamson and Hall plot, the crystallite size represented would be about 30.4 nm.

2.3 Film stress measurements and thin film mechanics

Basically there are two types of stresses in thin films, intrinsic and extrinsic. Intrinsic stress is a result of the deposition parameters. Extrinsic stresses are externally applied stress through straining or heating. In heating experiments stresses are caused as a result of the different coefficients of thermal expansion (CTE) in both the film and the substrate. This difference results in different desired expansions which can be balanced both elastically and plastically and result in a thermal stress [41].

There are different approaches to measure the stress in thin films. Diffraction methods such as the $\sin^2\Psi$ and the wafer curvature methods. Both were used in this work.

2.3.1 $\text{Sin}^2\Psi$-Method

The $\text{Sin}^2\Psi$ Method uses diffraction of monochromatic X-Rays to obtain stresses in crystalline materials. The strain of the crystal lattice is measured and the corresponding stress can be calculated using the material elastic constants [42]. The calculated stress directly resembles the stress of the film (absolute stress) and not the relative stress (consisting of film and substrate part). It is important to note that to obtain stress a crystalline microstructure is needed, amorphous microstructure would not produce the desired diffraction peaks. To improve the obtained data the experiments can be made with synchrotron radiation (SR). The advantages of using SR to conventional X-Ray sources is that the used beam has a significantly higher intensity, higher brilliance and high spatial resolution with better time resolution, therefore, making in-situ testing is possible. The main disadvantage is that SR is not as easily access able as conventional X-Ray sources.

The measurement relies on the well-known Braggs law [43].

$$\lambda = 2 * d * \sin(\theta) \tag{2.9}$$

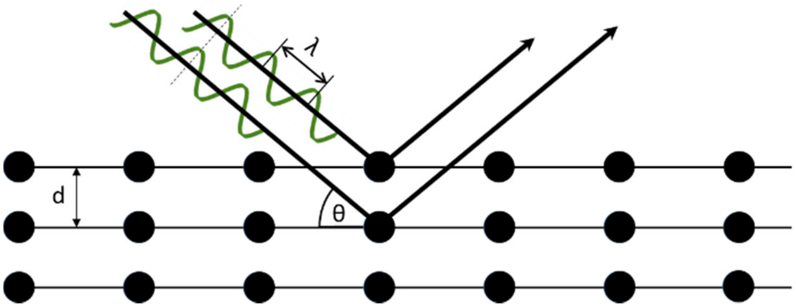

Figure 11: Schematic of Braggs law.

where *λ* is the wavelength of the X-ray beam, *d* is the interplanar distance and *θ* is the scattering angle. If the wavelength is known the interplanar distance can be calculated using the scattering angle. Differences in *θ* therefore are directly caused by differences in *d* as seen in Figure 12. Figure 12 a) shows the ideal unstressed lattice. Figure 12 b) shows the effect of compressive stress. It leads to increase of interplanar distance of the blue grain and therefore a shift of the corresponding blue peak to lower *θ* angles. The interplanar distances of the green grain get decreased leading to a shift to higher *θ* angles of the matching green peak. Figure 12 c shows the effect of tensile stress leading to increase of certain interplanar distances causing the peak-shift to lower *θ* angles and vice versa for the decreases.

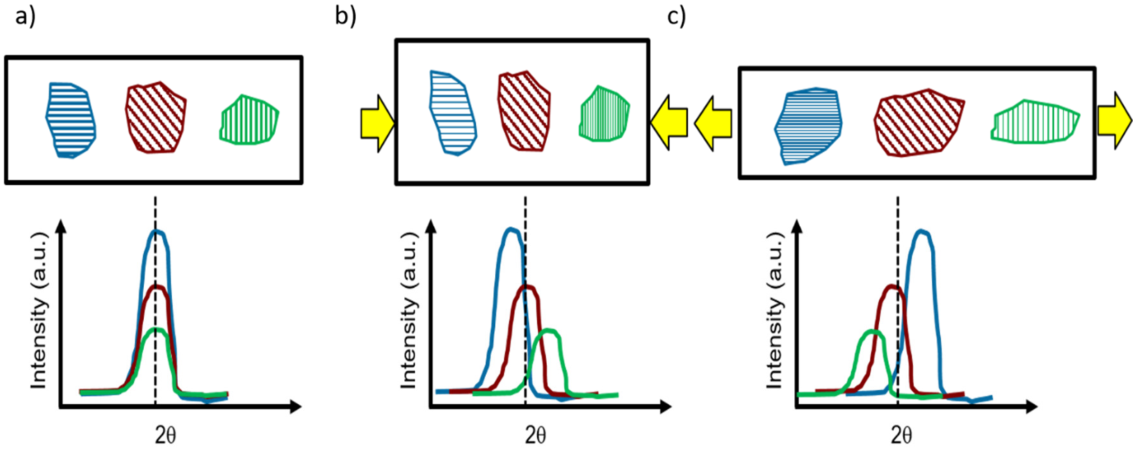

Figure 12: Shifting of diffraction peaks due to applying an external load. Decreases in the interplanar distance shifts the peaks to higher *θ* angles and vice versa for increases.

The lattice strains can then be calculated using the measured *2θ* angles [44]:

$$\varepsilon_\psi = \frac{d_{\phi\psi} - d_0}{d_0} = \frac{\Delta d}{d} = \frac{\theta_{\phi\psi} - \theta_0}{\tan(\theta_0)} = \frac{\Delta\theta}{\tan(\theta_0)} \tag{2.10}$$

If it is desired to know d_0, it has to be measured using unstressed samples or also can be found in literature [44]. The two sample method uses one sample with tensile and one with compressive stress. Two curves are obtainable, both similar to Figure 13 b, one with positive slope indicating the tensile stress and the other one with negative slope expressing the compressive stress. The point of intersection of both lines equals d_0.

Using the lattice strains the stress can be calculated using simple mechanics [42, 44] :

Hooke's Law:

$$\varepsilon_y = \frac{1}{E}\,\sigma_y \tag{2.11}$$

Assuming that there is biaxial stress and $\sigma_z = 0$ on the surface, where the measurement was made leads to [42]:

$$\varepsilon_z = -\nu\left(\varepsilon_x + \varepsilon_y\right) = -\frac{\nu}{E}\left(\sigma_x + \sigma_y\right) \tag{2.12}$$

Combining the equations leads to [42]:

$$\frac{d_n - d_0}{d_0} = -\frac{\upsilon}{E}\,(\sigma_x + \sigma_y) \tag{2.13}$$

To calculate the stress in a specific direction on the surface σ_Φ, elasticity theory for an isotropic solid has to be applied and leads to [42]:

$$\varepsilon_{\phi\psi} = \frac{1+\nu}{E}\left(\sigma_1\,cos^2(\phi) + \sigma_2\,sin^2(\phi)\right)sin^2(\psi) - \frac{\upsilon}{E}\,(\,\sigma_1 + \sigma_2) \tag{2.14}$$

With $\sigma_1 = \sigma_2$ and σ_3 it leads to the well-known equation:

$$\varepsilon_{\phi\psi} = \frac{1+\nu}{E}\;sin^2(\psi)\sigma - 2\frac{\upsilon}{E}\,\sigma \tag{2.15}$$

This resembles a linear equation:

$$y = k\,x + d \tag{2.16}$$

Therefore, one can simply take the slope of the curve as described in Figure 13 and calculate the stress using the following equation:

$$k = \tan(\propto) = \frac{1+\nu}{E}\,\sigma \tag{2.17}$$

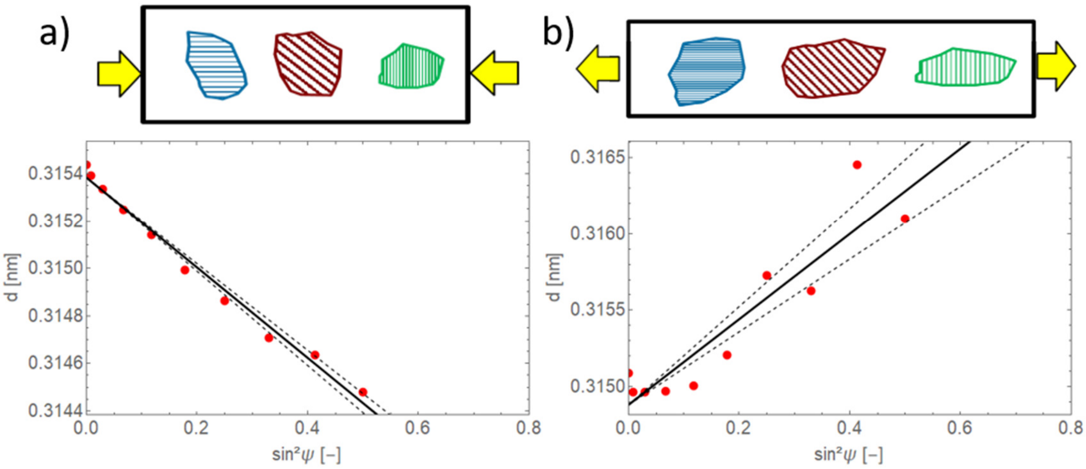

Figure 13: By plotting the measured d over the $\sin^2\Psi$ the stress can be calculated by measuring the slope and then using equation (2.17). a) corresponds to a compressive stress and therefore a negative slope and b) to tensile stress resulting in a positive slope.

2.3.2 Wafer Curvature

The wafer curvature method is based on the principle that if there is a mismatch in coefficient of thermal expansion (CTE) between the substrate and film the system will develop stress which results in a curvature. This curvature can, if the film is reflective, be measured by an alignment basically consisting of laser and sensor, which is calibrated to a known the position of the laser for different curvatures. This curvature is then used to calculate the stress using the well-known Stoney's equation [45].

$$\sigma = M_s \frac{h_s^2}{6h_f} * \left(\frac{1}{r_1} - \frac{1}{r_0}\right), \tag{2.18}$$

where σ is the stress, M_s and h_s are the biaxial modulus and thickness of the substrate, h_f is the film thickness, r_0 and r_1 are the curvature of the substrate before deposition and the measured curvature during the experiment, respectively [45, 46]. This method in contrast to the $\sin^2\psi$ method calculates relative stress. If the absolute stress has to be known, the curvature of substrate itself has to be measured and subtracted from the curvature of the film substrate compound at respective temperature. Since the only requirement for the film in this method is that the surface reflects properly also amorphous materials like metallic glass films, which would not be measurable with the $\sin^2\psi$ method, can be measured.

The used setup uses two Fabry-Pérot interferometer to create a 4x4 laser grid. This grid is then reflected by the sample surface and a Multi-Beam Optical Sensor (MOS) System by k-Space Associates is used to observe the change in position of every spot [47]. The sample is placed on a heating plate and not only the residual stress but also the thermo-mechanical behaviour is obtainable.

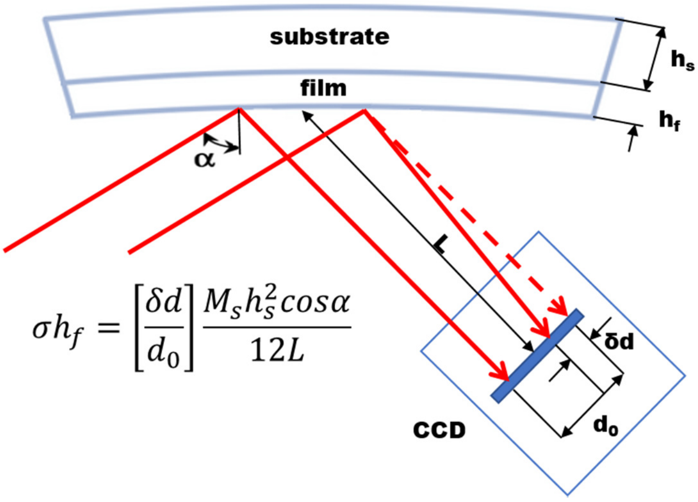

Figure 14: Wafer curvature setup as described in the text analogous to [48] taken from [47] with permission.

An example of a typical curve obtained by a wafer curvature setup is shown in Figure 15, it shows a typical curve for Mo-Ag thin film on Silicon. The stress at the beginning of the thermo-cycle point (I) is a direct result of the deposition process [46]. While heating the stress falls linearly until reaching point (II), where the curve leaves the thermo-elastic line [46]. After leaving this line the film starts to deform non-elastically, plastic deformation can be caused by different mechanisms such as grain growth, gliding of dislocations and relaxation of the grain boundaries [46]. As a result of heating creep processes are activated and the creep velocity increases [46]. At point (III), which is usually followed by a plateau or slight decrease of stress (IV), the creep strain, the thermo-elastic strain and possibly material compaction compensate each other. Point (III) is often characterised by the minimal stress [46]. While holding at a certain temperature for a longer time (some minutes) it was seen that stress in most of the cases increased. This can be attributed to various temperature and time dependent effects such as grain growth, changes in dislocation structure and similar effects attributed to diffusion such as segregation of compounds.

While cooling down a thermo-elastic line can be detected again while the stress increases (V) [46]. Stress increases with decreasing temperature (VI), while creep-velocity also decreases, this could lead to more rounded curves as described in Figure 15 [46]. The heating cycle ends (VI) with a significant higher stress compared to the initial stress (I) [46].

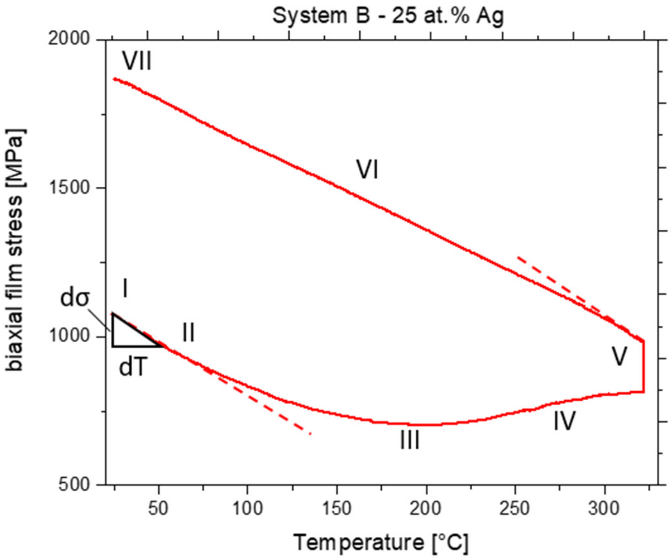

Figure 15: Typical thermal evolution of stress of a Mo-Ag thin film on Silicon.

Characterisation of the temperature dependence of the elastic region is done by treating the linear decrease in stress as a purely elastic phenomenon [49]. Therefore, a few theoretical considerations have to be taken account of as described in [50]. To calculate the stress slope following equation was used.

$$\frac{d\sigma}{dT} = \Delta\alpha * \frac{E}{1-\upsilon} \tag{2.19}$$

E and υ are the Young's modulus and the Poisson's ratio of the film.

The used CTE for the different materials was taken from the listed literature:

$$\alpha_{Si} = 3.056\ 10^{-6}\ 1/K\ [51]$$

$$\alpha_{Mo} = 5.2\ 10^{-6}\ 1/K\ [52]$$

$$E_{Mo} = 320\ GPa\ [52]$$

$$\upsilon_{Mo} = \ 0.31[52]$$

$$\alpha_{Ag} = 19.7\ 10^{-6}\ 1/K\ [53]$$

$$E_{Ag} = 79\ GPa\ [54]$$

$$\upsilon_{Mo} = \ 0.38\ [54]$$

This leads to -0.994 MPa/K for Mo on Si and -2.12 MPa/K for Ag on Si. All of the used constants are dependent on the interatomic potential. This means by changing the potential through any means, e.g. alloying, the constants will vary changes should be obtainable. In general the calculated values can be taken as a reference slope for texture-less pure Mo or pure Ag film [50].

3 Materials and Experiments

All the experiments were performed on Molybdenum-Silver (Mo-Ag) alloy films. They were synthesized by a laboratory-scale unbalanced dc Magnetron sputtering process. The sputtering was current controlled co-sputtering with two Mo targets with 0.35 A and one Ag target with varying dc current. The Argon pressure was ~0.38 Pa. The films were fabricated by T. Jörg (Department of Functional Materials and Material Systems, Montanuniversität Leoben) using the deposition parameters outlined in Table 1, Table 2 and Table 3.

Two different substrates were used: a 350 µm thick Silicon and 50 µm Polyimide (Upilex®-S). The film systems will be called System A for the thin films on Silicon ranging from 40 nm to 55 nm, System B for thicker films on Silicon ranging from 400 nm to 770 nm and System C for films on Polyimide ranging from 40 nm to 55 nm. The film thicknesses were determined by the known deposition rate and verified with atomic force microscopy (AFM) or focused ion beam (FIB) cross-sections. All the Polyimide films where strained in previous experiments by T. Jörg up to 15% strain before the experiments described in this thesis were carried out. Tables 1 – 3 summarize the samples used in this thesis.

Table 1: System A thin films on Silicon

System A				
Composition	**Thickness [nm]**	**Current [A]**		**Deposition time [sec]**
		Mo	**Ag**	
$Mo_{91}Ag_{9}$	55	0.7	0.02	56
$Mo_{82}Ag_{18}$	50	0.7	0.05	37
$Mo_{75}Ag_{25}$	40	0.7	0.07	33
$Mo_{69}Ag_{31}$	35	0.7	0.1	30
$Mo_{56}Ag_{44}$	50	0.7	0.15	31
$Mo_{48}Ag_{52}$	40	0.7	0.2	25
$Mo_{41}Ag_{59}$	55	0.7	0.25	25

Table 2: System B thicker films on Silicon

System B				
Composition	**Thickness [nm]**	**Current [A]**		**Deposition time [min]**
		Mo	**Ag**	
$Mo_{91}Ag_9$	400	0.7	0.02	8
$Mo_{82}Ag_{18}$	580	0.7	0.05	8
$Mo_{75}Ag_{25}$	560	0.7	0.07	8
$Mo_{69}Ag_{31}$	640	0.7	0.1	7
$Mo_{56}Ag_{44}$	760	0.7	0.15	8
$Mo_{48}Ag_{52}$	770	0.7	0.2	6

Table 3: System C films on Polyimide

System C				
Composition	**Thickness [nm]**	**Current [A]**		**Deposition time [sec]**
		Mo	**Ag**	
$Mo_{91}Ag_9$	55	0.7	0.02	56
$Mo_{82}Ag_{18}$	50	0.7	0.05	37
$Mo_{75}Ag_{25}$	40	0.7	0.07	33
$Mo_{69}Ag_{31}$	35	0.7	0.1	30
$Mo_{56}Ag_{44}$	50	0.7	0.15	31
Ag	50		0.35	20

The thermo-mechanical characterisations where performed with a wafer curvature system used for in-situ film stress measurements up to 1000°C at a pressure of $\sim 10^{-4}$mbar. To measure the evolving film stress an optical beam sensor from kSA MOS (k-Space Associates, Inc. Dexter, 48130 USA) was used [55]. The experiments were performed at two different maximum temperatures of approximately 300°C and 400°C. Each experiment was performed for one cycle with the heating and cooling rates set to 10K/min. The cycles started at room temperature and the cooling was completed to about 40°C, since further cooling would need external cooling to ensure the 10k/min. The maximum temperature was held for 1h to enhance the possibility of microstructural evolution or diffusion processes. The temperature correction of the wafer curvature system was described by [47].

The temperature treatments for the films on Polyimide where done in an vacuum tube furnace at 350°C for 2h with an ramp rate of 10K/min at about $\sim 10^{-4}$mbar.

To characterise the films before and after straining or heating experiments, a scanning electron microscope (SEM) LEO 1525 (Zeiss Inc., Oberkochen, Germany) and a laser confocal scanning microscopy (CLSM - Olympus LEXT OLS 4100) were used.

All X-Ray data, if not declared to be from another source, was obtained in January 2018 at BESSY II at the KMC-2 beamline. The beamline was an diffraction station, using a 6-circle diffractometer from Huber, a 2D-detector with a gas filled wire by BRUKER AXS with an active area of 115 mm in diameter and an energy range from 3-15 keV was used [56]. For further information on the beamline see [57]. All the measurements were done at the wavelength of CuK_α (1.5406 Å). The $\sin^2\Psi$ scans were made by moving the chi angle from 90° to 45° with 9 steps (10 measurements total) with 15 seconds holds at each position [56]. The θ-2θ scans were made by moving the del angle from 35° to 95° and the eta angle from 17.4° to 47.5° with 30 steps (31 measurements total) with 11 seconds holds at each positon [56]. On samples of System A the $\sin^2\Psi$ was applied in two directions after one or two Wafer curvature treatments as seen in Table 4. On samples of System B both $\sin^2\Psi$ and θ-2θ scans were used for characterisation.

Table 4: Sample overview. WC = Wafer curvature. All heating rates were 10 K/min. Slipped means the sample wasn't fixed properly in the straining device, leading to slipping during the tensile testing. Broken means sample broke before reaching 12% strain.

Substrate	**Si**			**PI**		
System	**System A**		**System B**	**Sytem C**		
Compositon	**WC**		**WC**	**Strained**	**annealed**	**Strained insitu LEXT**
$Mo_{91}Ag_{9}$	1h 320°C	-	1h 320°C	15%	2h 350°C	Slipped
$Mo_{82}Ag_{18}$	1h 320°C	-	1h 320°C	15%	2h 350°C	Broken
$Mo_{75}Ag_{25}$	1h 320°C	-	1h 320°C	15%	2h 350°C	12%
$Mo_{69}Ag_{31}$	1h 320°C	1h 400°C	1h 320°C	15%	2h 350°C	12%
$Mo_{56}Ag_{44}$	1h 320°C	1h 400°C	1h 320°C	15%	2h 350°C	Broken
$Mo_{48}Ag_{52}$	1h 320°C	1h 400°C	1h 320°C	-	-	-
$Mo_{41}Ag_{59}$	1h 320°C	-	didn't reflect	-	-	-
Ag	-	-	-	15%	2h 350°C	insitu @Bessy

4 Results

All portions of data if not specifically marked as performed by Tanja Jörg were completed by the author of this thesis.

4.1 Rigid Substrates

XRD was initially used to determine the chemistry of the as deposited thin films (performed by T. Jörg after film deposition). After that the films were annealed using a wafer curvature set up, measuring the thermal stress evolution of the film. Synchrotron radiation was then used to identify changes in the chemistry and to obtain information the about residual stress in the films.

Figure 16 shows the significant parts of all compositions of Mo-Ag including a pure Mo and a pure Ag film for comparison. One can see that the increasing percentage of the larger Ag atoms with 160 pm [58] compared to Mo with 154 pm [58] shifts the Mo (110) peaks to lower 2Θ angles in the direction of Ag (111). Starting with 44 at.% Ag the Mo (110) peak broadening becomes more pronounced and the shifting to lower angles becomes obvious. The Mo (200) peak is clearly obtained until 31 at.% Ag.

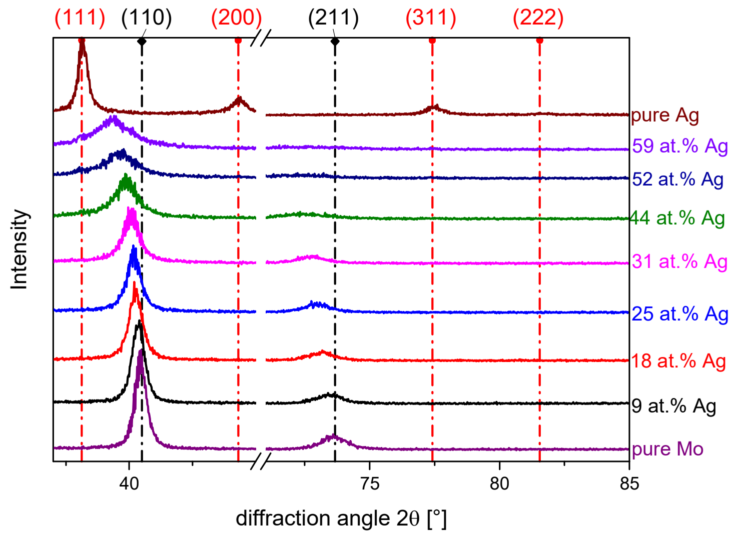

Figure 16: θ-2θ scan of System A films in the as-deposited state. The red-dashed-lines indicate Silver peaks and the black Molybdenum. Raw data of the graph from Tanja Jörg.

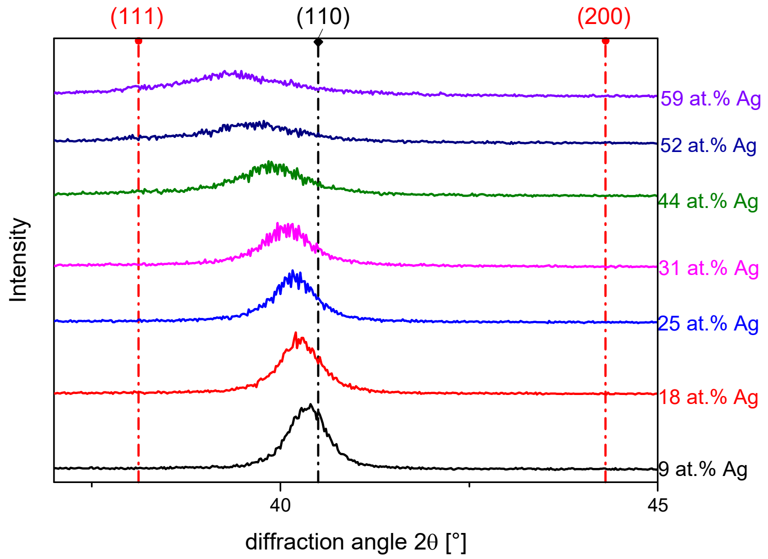

Figure 17: Detail of Figure 16 .The red-dashed-lines indicate Silver peaks and the black Molybdenum.

4.1.1 Film stress

Film stress was measured with different complimentary techniques to be able to identify trends during variation of the Ag composition.

4.1.1.1 Thermal stress evolution

The wafer curvature method was used to obtain the evolution of stress in System A and System B (thin and thick films on Si). Both Systems were annealed to 320°C for an hour with a heating rate of 10 K/min. System A 31 at.% Ag, 44 at.% Ag and 52 at.% Ag where additionally heated to 400°C with an holding period of 1h to enhance microstructural changes as well as segregation, as described in Table 4.

By comparing the Figure 18 a) to g) one can see that thicker films contain higher intrinsic (residual) stresses, at the beginning and at the end of the cycle. All of the films cycled to 320°C, except of System A 9 at. % Ag, showed an increase of stress during the holding period. Figure 18 a) and b) show mostly elastic behaviour compared to the rest of the figures, which show pronounced rounding of the curves at elevated temperatures indicating plastic deformation process are occurring. All the films which were additionally cycled to 400°C show a decrease of stress during the holding period but in the rest of the cycle mostly elastic behaviour. This lack of pronounced rounding of the curves indicates that more thermal cycling doesn't result in more plastic deformation. Figure 18 g) only shows a slight increase in stress during holding time at 320°C.

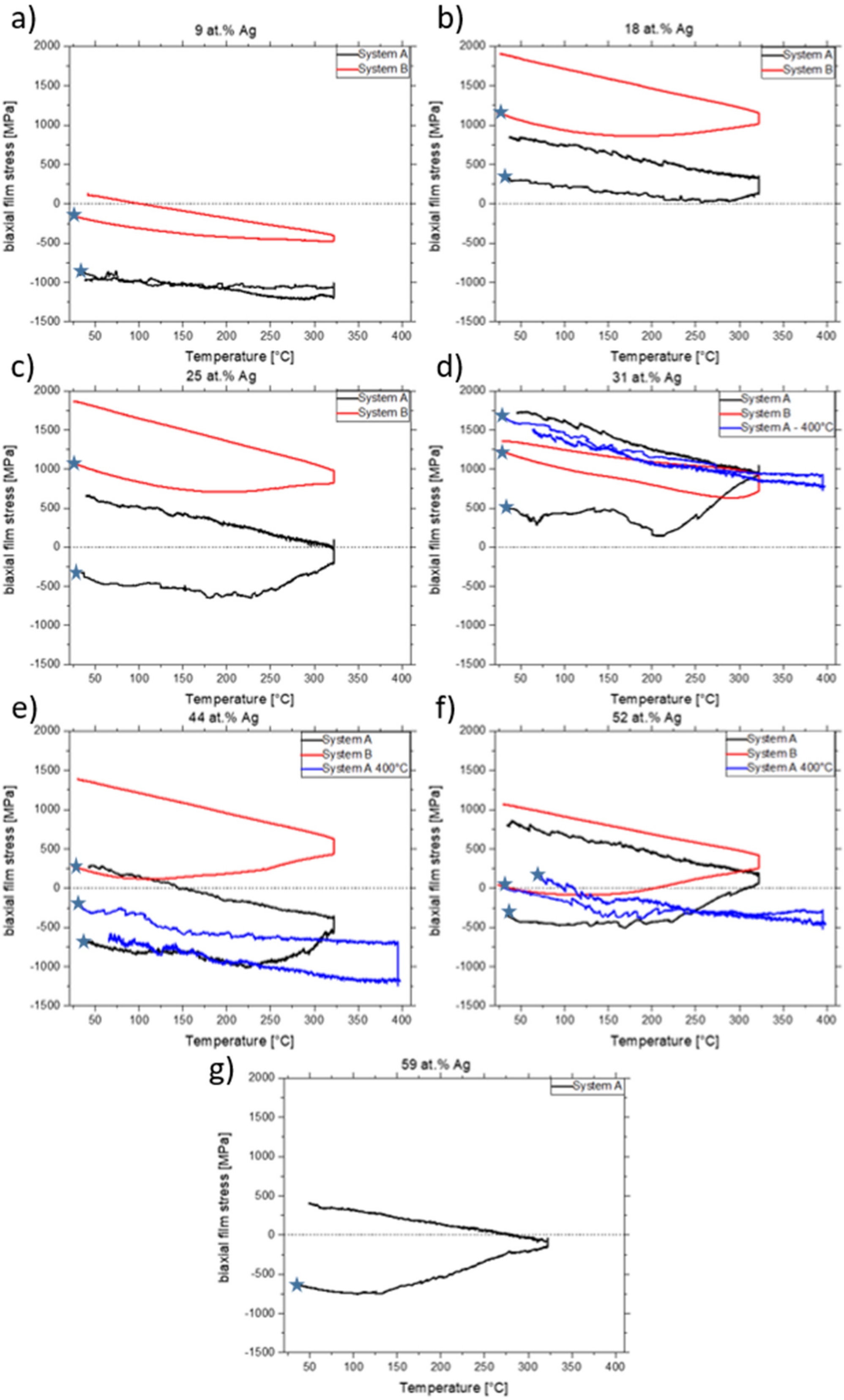

Figure 18: Thermal stress evolution of System A and B. Stars indicate the start of the cycle.

Figure 19 shows an overview over all compositions of System B one can see that 9 at. % Ag shows negative (compressive) stress at the beginning and slightly positive (tensile) stress after the cycle. 18 at.% and 25 at.% Ag show similar curves in terms of achieved stress. For 31 at.% Ag the stress before and after the cycle differ the least of all and it starts higher than all the others but it does not increase in a similar way than the other ones. Instead it even shows a decrease after the thermo-elastic line of cooling. 44 at.% Ag starts with a significantly lower stress than 18 – 31 at.% Ag but drastically increases, it also shows pronounced non elastic effects. 52 at. % shows nearly no stress at the beginning but similar to 44 % it shows pronounced non-elastically behaviour after the thermo-elastic line at heating.

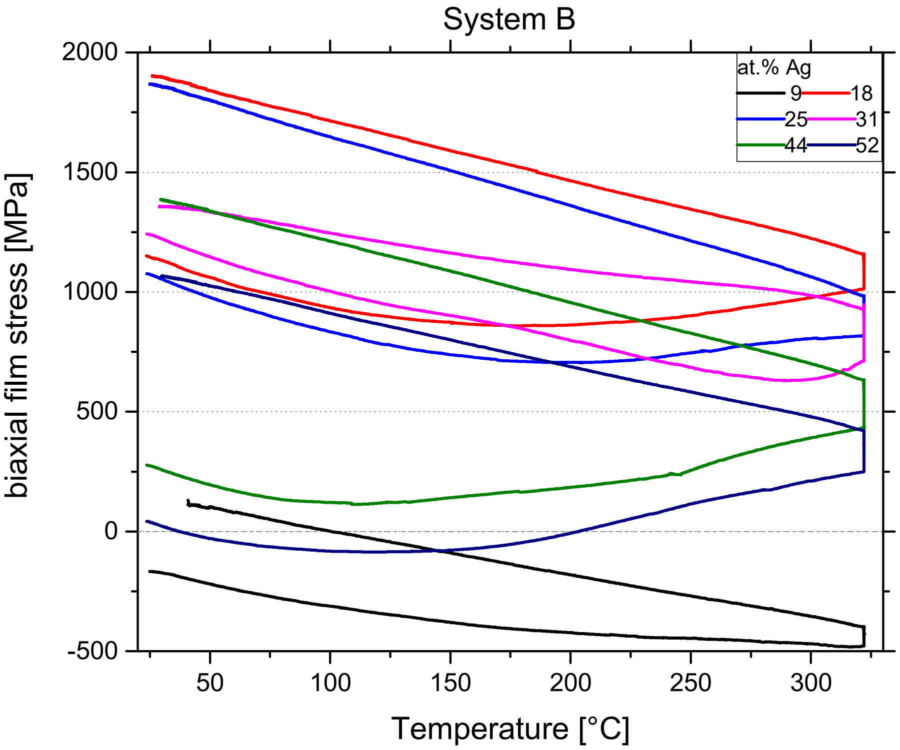

Figure 19: Overview over all compositions of System B the trends after annealing are described by Figure 20, the evolution of the thermo-elastic lines is described in Table 5

To produce the following Tables MatLab Curve Fitting Tool with Polynomial Fitting of the first degree was used. RMSE means Root Means Squared Error and is a description of how well the data was fit. System B (see Figure 19) was used for evaluation, since it was found to have less noise as the thinner films, therefore making the values easier to evaluate and to compare. Both the heating and the cooling slopes show the same behaviour. The dσ/dT is becoming more negative until 25 at.% Ag and starting with 31at. % Ag the values begin to increase again (Table 5).

Table 5: *dσ/dT* for heating of System C in the regime of 35°C-55°C and *dσ/dT* for cooling of System C in the regime of 320°C-300°C, RMSE means Root Means Squared Error of the fit

Composition	**heating**		**cooling**	
	dσ/dT $[\frac{MPa}{K}]$	**RMSE**	***dσ/dT*** $[\frac{MPa}{K}]$	**RMSE**
9 at.% Ag	-2.414	0.483	-2.096	0.7233
18 at.% Ag	-3.317	1.816	-3.117	0.8756
25 at.% Ag	-3.635	0.6617	-3.812	1.074
31 at.% Ag	-3.558	0.6798	-2.718	1.319
44 at.% Ag	-2.938	0.8031	-3.214	1.179
52 at.% Ag	-2.245	0.9469	-2.745	0.9916

Figure 20, and Figure 21 show the evolution of the stresses before and after the wafer curvature treatment near to room temperature. The figures show an increase of stress for the 320°C annealing up to 31 at.% Ag and an decrease afterwards. This is observed for both System A and System B. By comparing the before and after values in Figure 20 one can see that the trend stays the same, but gets more pronounced after annealing for the thinner films. Also, all the stresses shift to higher values after the heat treatment. Figure 21 shows that the stresses after the additional annealing to 400°C decreased, this can also be seen in Figure 18 d)-f) where the films even exhibit a decrease in stress during the 1h holding period.

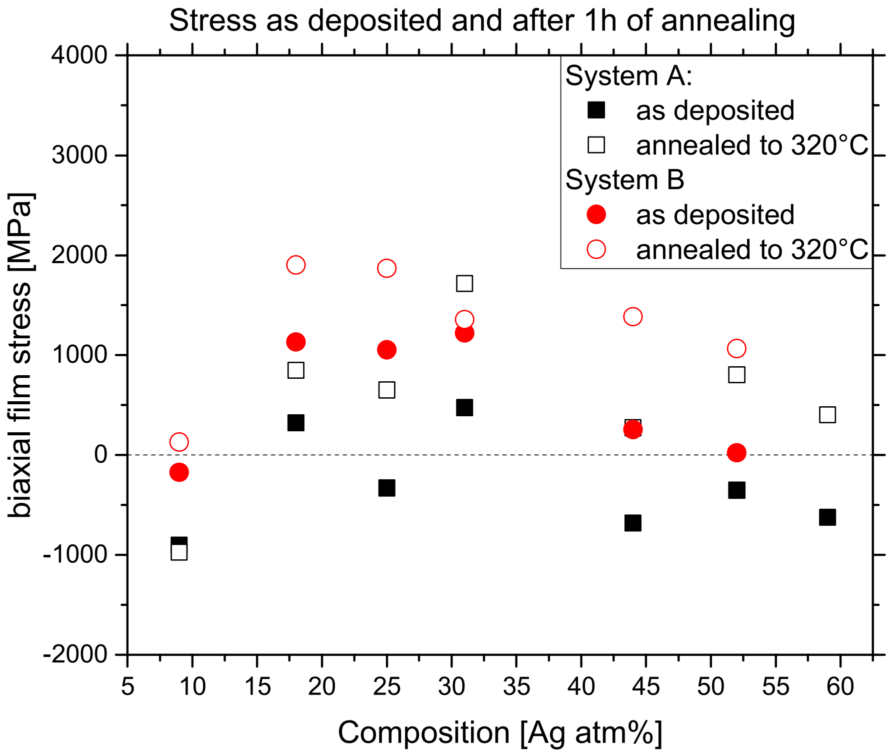

Figure 20: Stress before and after annealing treatment of 1h to 320°C for System A and System B

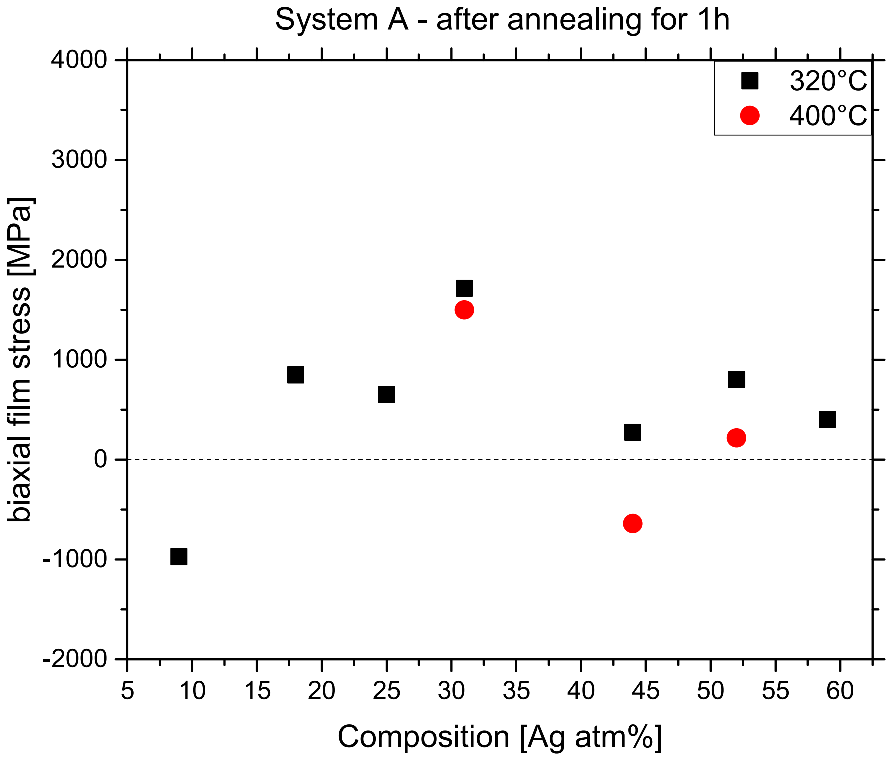

Figure 21: System A Stress evolution after annealing treatment for 320°C and additional 400°C

4.1.1.2 Sin^{2}Ψ-Method

Figure 22 shows plots of stresses obtained by the sin^{2}ψ method at the Synchrotron Bessy II in Berlin. Phi 0 means that the stress is measured on the long side of the sample and Phi 90 means that the stress is measured on the smaller side of the sample (the sample is rotated by 90°). By comparing the values for the different phi angles in Figure 22 one can see that the residual film stresses in both directions follow the same trend and have overall similar values. This means that the measured stresses are equi-biaxial. When following the trend one can see that until a composition of 31 at.% Ag the stress in Mo increases and after that at 44 at.% Ag the stress decreases dramatically. This is also the turning point for the solid solution chemistry for the Mo-Ag. The Ag stress measured for two crystallographic planes remains constant over all the compositions. Peaks were only measured when fully obtained over all measured profiles. For System A 44 at.% less profiles were produced due to a problem at the beamline, therefore the error bars increased, but the overall trend stayed the same. Note that all but 31 at.%, 44 at.% and 52 at.% were only annealed once to 320°C for one hour, the other named ones were annealed additionally to 400°C for an additional hour as seen in Table 4. When comparing the mentioned figures to Figure 21 one can see that the same trend is clearly visible in the wafer curvature data and the X-Ray data.

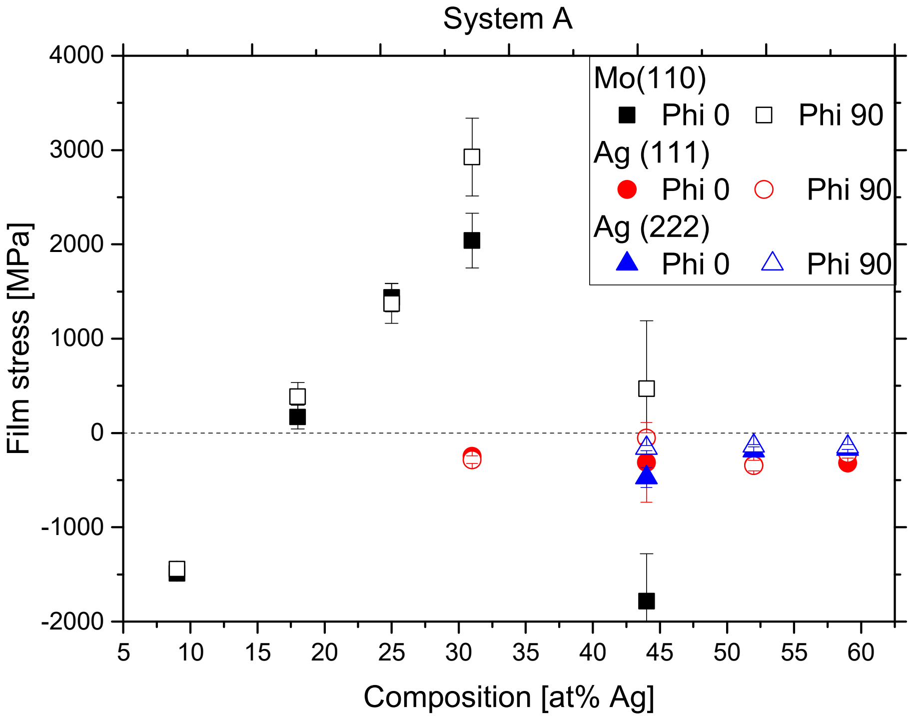

Figure 22: Film stress evolution of System A. After annealing treatments as described by Table 4.

4.1.2 Surface Features after Annealing

The *θ-2θ* scan of System A after the annealing treatments is shown in Figure 17. When comparing Figure 17 and Figure 23 one can see that the peaks starting with 31 at.% Ag show distinct signs of separation of Mo-Ag to a Molybdenum rich and an Silver rich phase. This is accompanied with a shift of the peaks to the theoretical values of pure Mo and Ag and the appearance of an additional (111) Ag peak. Also, the Ag (200) peak is detected for these compositions. At lower Silver percentages up to 25 at.% Ag not much seems to have changed, this is an indication for a stable Mo-Ag solid solution.

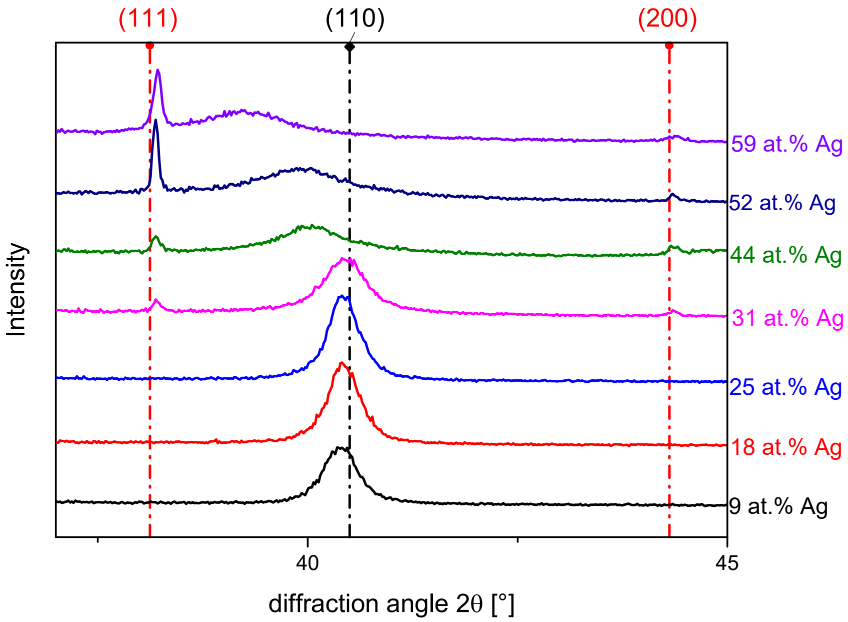

Figure 23: *θ-2θ* scan of System A annealed. All compositions were annealed to 320°C for 1h and 31 to 52 at.% Ag where additionally annealed up to 400°C for 1h to enhance segregation and microstructural evolution, for details see Table 4. The red-dashed-lines indicate Silver peaks and the black Molybdenum.

9 at.% Ag

Figure 24 shows that only a few Ag-rich particles form on the surface after annealing to 320°C for 1h.

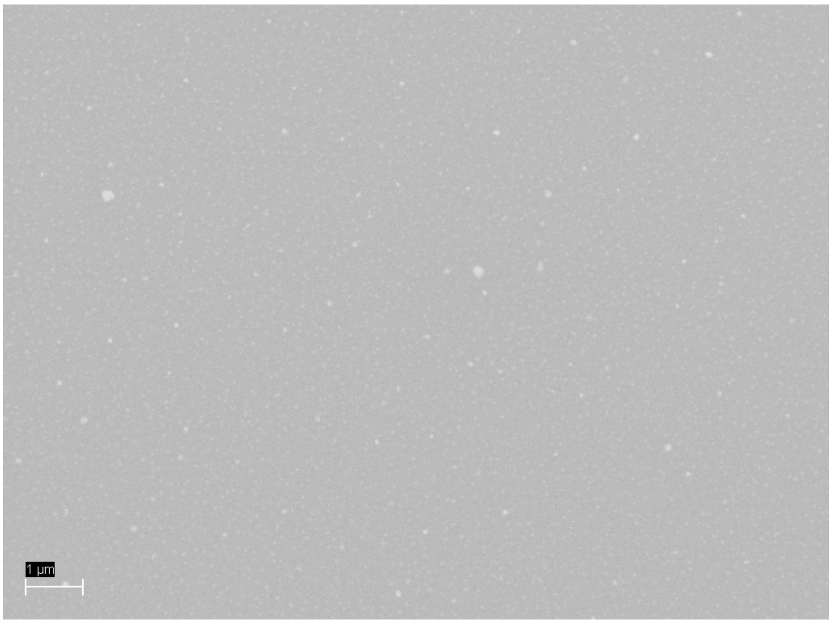

Figure 24: 9 at.% Ag of System B after annealing to 320°C for 1h

18 at.% Ag

Figure 25 shows that only a few Ag-rich particles form on the surface after annealing to 320°C for 1h.

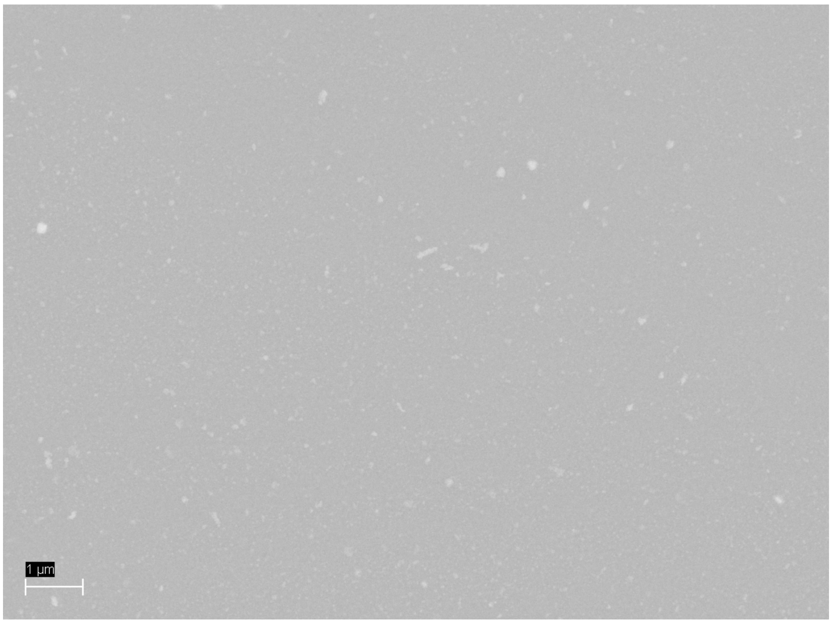

Figure 25:18 at.% Ag of System B after annealing to 320°C for 1h

25 at.% Ag

Figure 26 shows that Ag-rich particles form on the surface after annealing to 320°C for 1h.

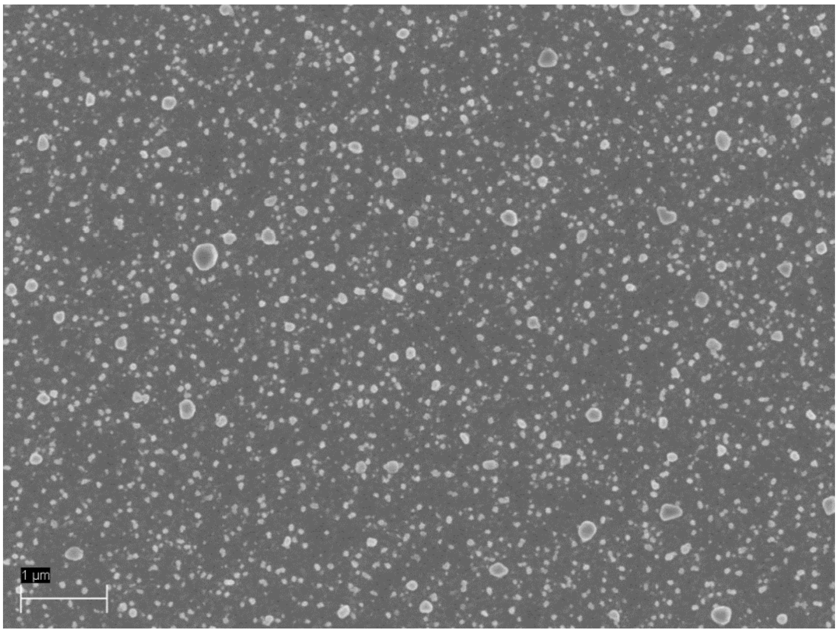

Figure 26: 25 at.% Ag of System B after annealing to 320°C for 1h

31 at.% Ag

Figure 27 shows that Ag-rich particles form on the surface after annealing to 320°C for 1h. And after an additional annealing as seen in Figure 28 the particles seem to have an overall more rounded shape.

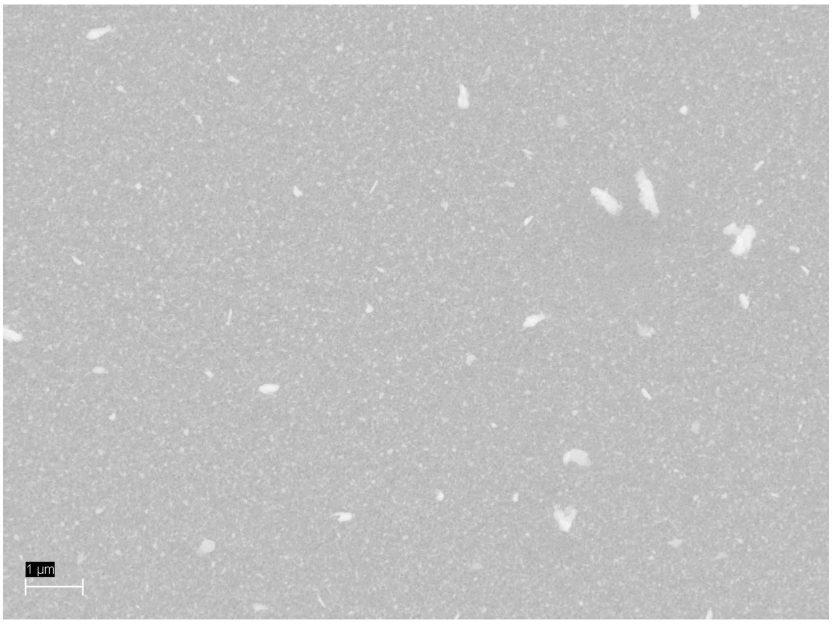

Figure 27: 31at.% Ag of System B after annealing to 320°C for 1h

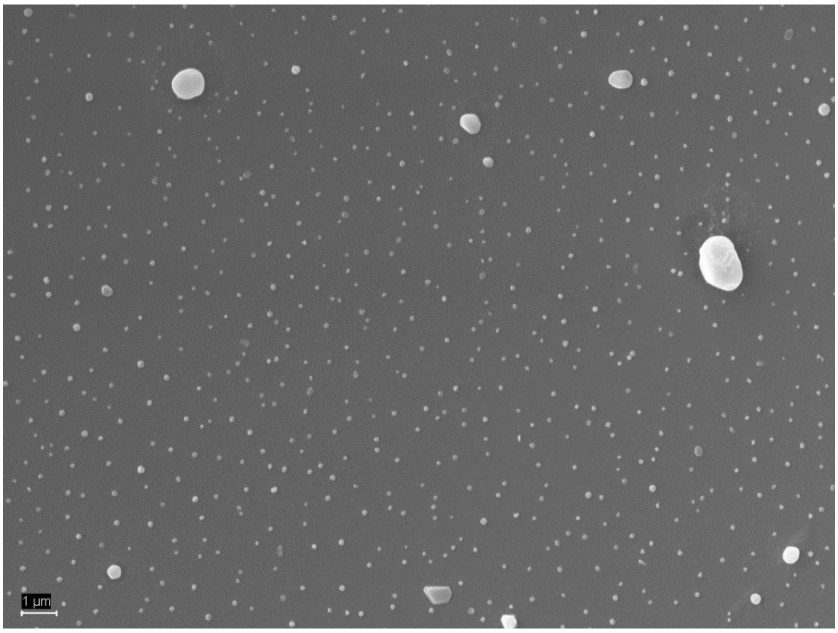

Figure 28: System A 31 at% after the additional annealing to 400°C 1h

44 at.% Ag

Figure 29 shows the as deposited 44 at.% Ag film, Ag-rich particles seem already to have formed on the surface, they are evenly distributed and have various shapes and sizes. After annealing to 320°C for 1h (Figure 30) the particle size seems to have increased and the shape seems to have shifted to more rounded particles. After the additional annealing shown in Figure 31 the particles seem to be even rounder and they seem to have a tendency for clustering.

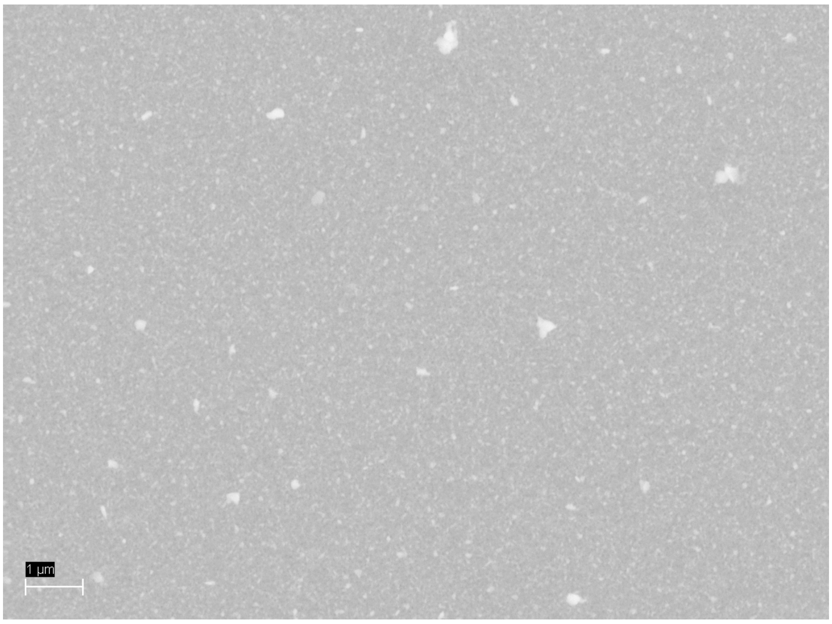

Figure 29: 44 at.% Ag of System B as deposited

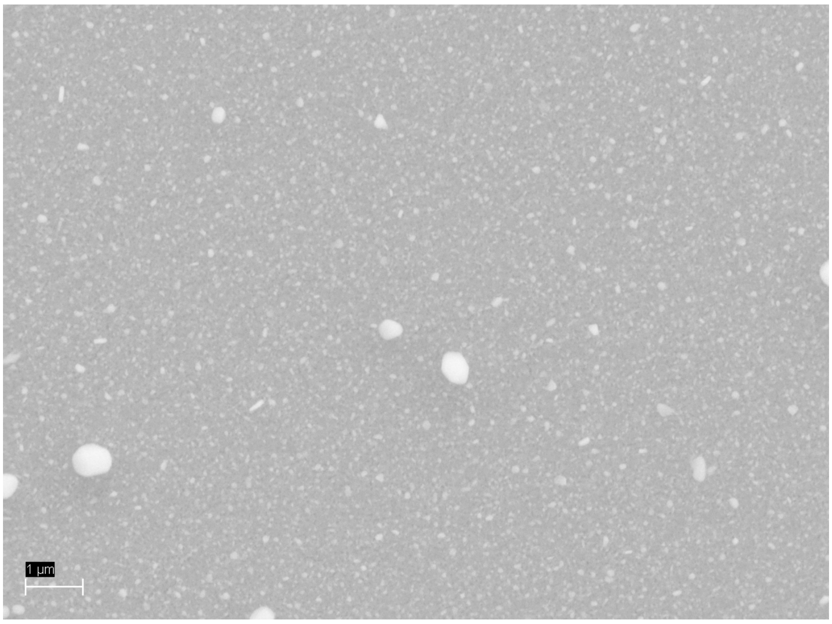

Figure 30: 44at.% Ag of System B after annealing to 320°C for 1h

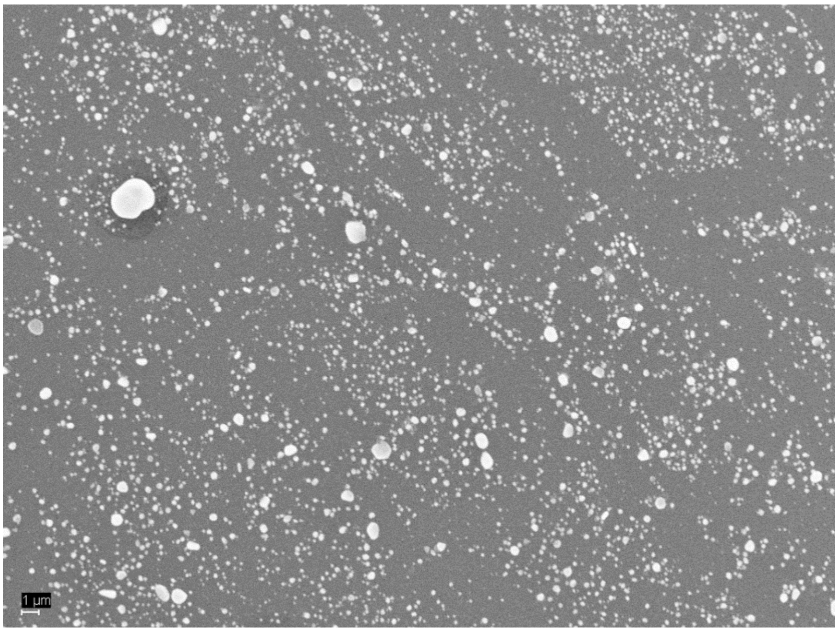

Figure 31:System A 44 at.% Ag after the additional annealing up to 400°C 1h

52 at.% Ag

In Figure 32 and Figure 33 suggest that the particles again are various shapes and sizes after annealing to 320°C and after 400°C the shapes shift to more rounded ones. The particle distribution changed to less but larger particles.

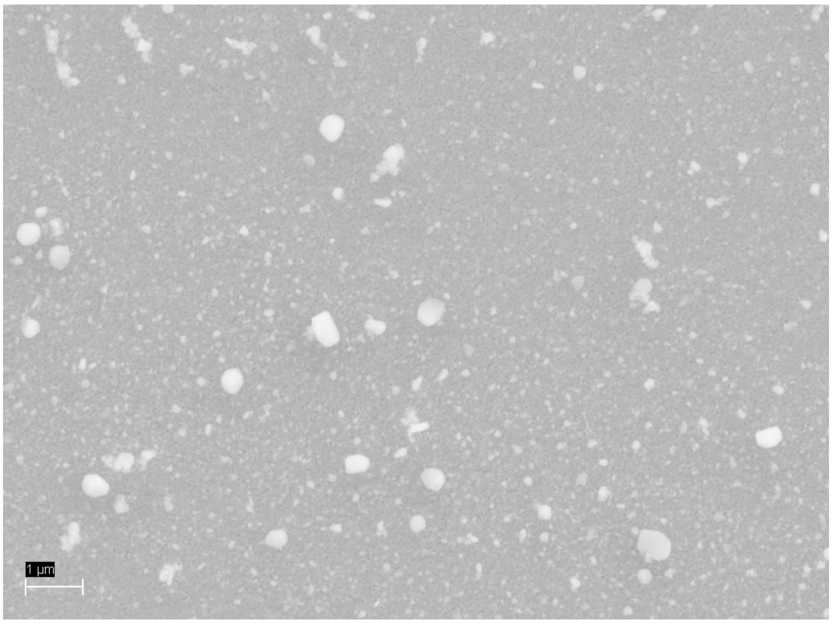

Figure 32:52 at.% Ag of System B after annealing to 320°C for 1h

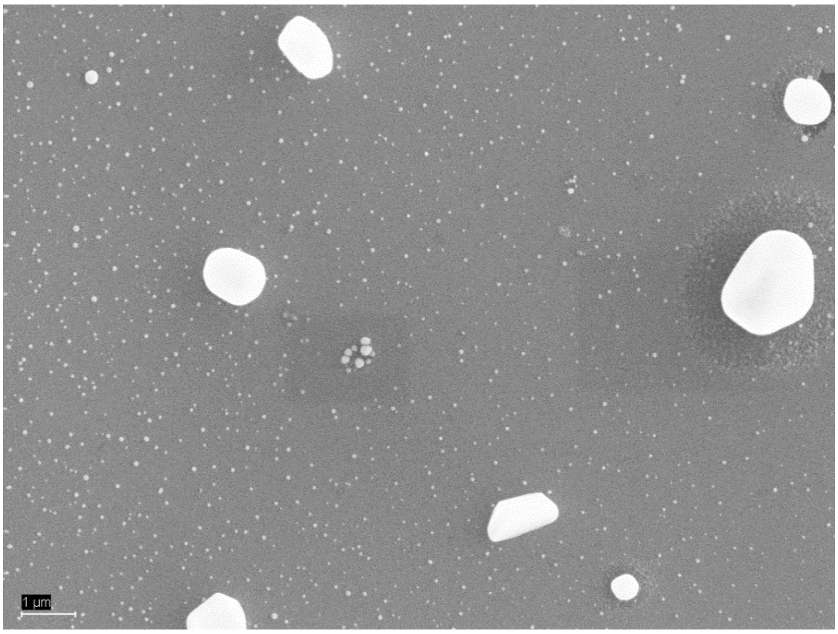

Figure 33:System A 52 at.% Ag after additional annealing to 400°C for 1h

4.2 Flexible Substrates

The films were deposited on Polyimide to enable straining of the films. Annealing was performed to characterize if and where Ag rich phases segregate on the film surface. To emphasize this and to be able to compare it to the rigid samples stresses where measured and *θ-2θ* scans (crystallite size) where performed after annealing to 350°C for 2h.

When comparing Figure 23 to Figure 34 one can see that in Figure 34 the separation of Mo-Ag to a Mo rich and an Ag rich phase is only obvious in 44 at.% Ag. This is a direct result of the different annealing steps performed on the different systems, for details see Table 4. System B was annealed to 350°C for 2h since higher Temperatures might cause the Polyimide substrate to melt. The Mo (220) peak is obtainable in all samples up to 44 at% Ag and the (211) peak up to 31 at.% Ag.

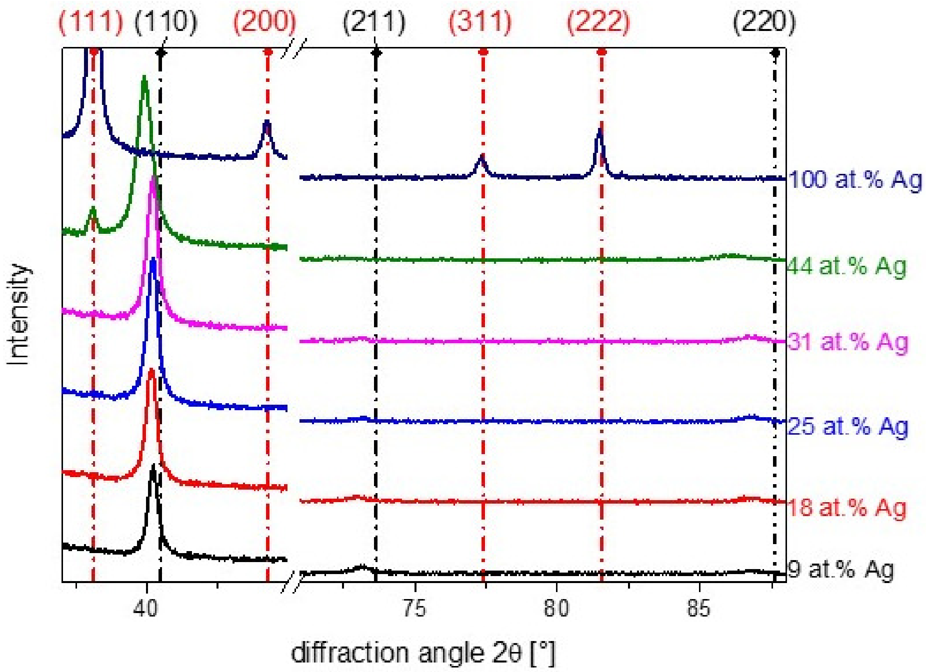

Figure 34: *θ-2θ* of System C after straining to 15% and annealing to 350°C for 2h as described by Table 4. The red-point-dashed-lines indicate Silver peaks and the black Molybdenum.

4.2.1 Crystallite size estimation

4.2.1.1 Mo crystallite size

Table 6 shows the calculated crystallite size for Mo peaks obtained with different methods. The data of Figure 34 was used to perform the calculations. The Scherrer method shows an overall nearly constant average crystallite size, while the Williamson-Hall method which tries to separate the micro-strain broadening from the crystallite-size broadening, varies quite a bit. This might be due to the small amount of peaks which were measured since the Williamson Hall method should get more precise when more peaks are taken into account.

Table 6: Crystallite size of Mo determined by different calculation methods for strained and annealed System C. The instrumental broadening is taken account of. For the Williamson and Hall Method the Instrumental Broadening Lorenz shape of the peak is assumed. Scherrer constant is assumed as 0.9.

at.% Ag	Scherrer Average [nm]	Williamson-Hall [nm]
9	17.1±6.9	69
18	18.6±5.2	31
25	19.8±5.4	66
31	17.8±5.5	31
44	12.6±4.3	92

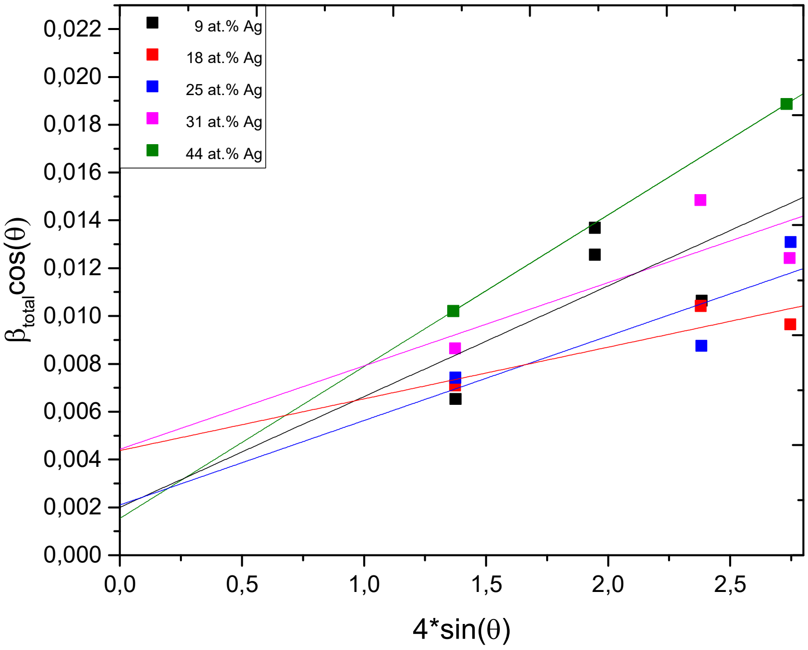

Figure 35: Williamson-Hall Plot of System C for Molybdenum peaks. Every dot represents one peak as described by Figure 34.

4.2.1.2 Ag crystallite size

Table 7 shows the calculated crystallite size for Ag peaks obtained with different methods. The data of Figure 34 was used to perform the calculations. The Scherrer method shows an overall nearly constant average crystallite size.

Table 7: Crystallite size of Ag for strained and annealed System C. The instrumental broadening is taken account of. Scherrer constant is assumed as 0.9. Note that for 44 at. % Ag only one Peak was obtainable (see Figure 34 for detail).

at.% Ag	Scherrer
	Average [nm]
44	46.6±
100	57.2±18

4.2.2 Film stress measurement

Figure 36 shows the evolution of stress in System C it shows overall the same trend as described for both System A and B, although the overall stress was found to be compressive in all samples. The milder decrease at 44at. % Ag compared to Figure 22 might be attributed to the different temperature treatment (described in Table 4), heating to 400°C seems to accelerate the microstructural changes and segregation, leading to a faster decrease in stress this can be seen in Figure 21.

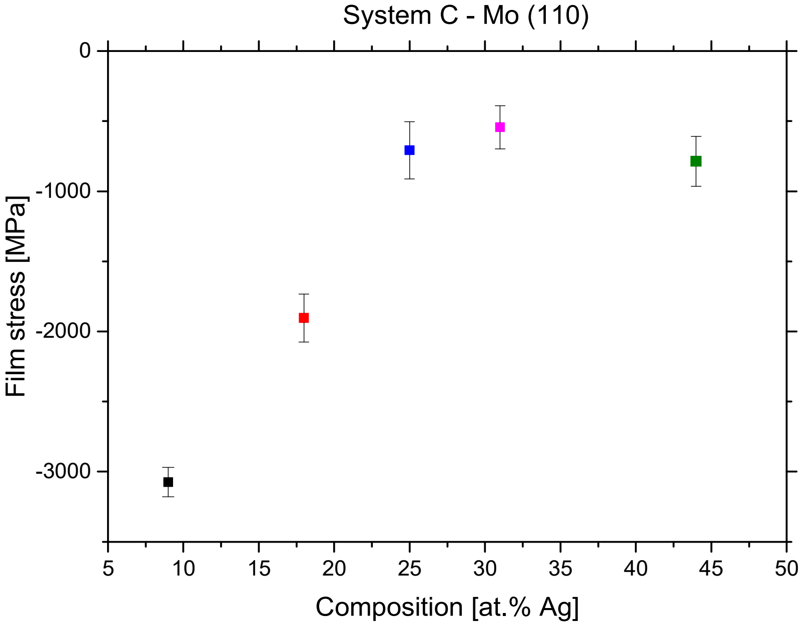

Figure 36: Evolution of film stress in System C for strained and then annealed samples. Calculated using the Sin$^2\Psi$-Method on the (100) peaks of Molybdenum

By applying Equation (4.1) one can see that for *ΔT=325°C* $\alpha_{PI,T=350°C} = 27.8\,ppm/°K$ [59], and the values used for Mo in chapter 2.3.2 the film stress should be around -3400 MPa if the stress in the substrate is not considered. Therefore the negative values in Figure 36 are valid and in the right range.

$$\sigma = \frac{(\alpha_{Mo} - \alpha_{PI}) * \Delta T * E_{Mo}}{1 - \vartheta_{Mo}} \tag{4.1}$$

4.2.3 Surface features after annealing

All the samples were strained to 15% elongation and afterwards annealed to 350°C for 2h. Most of the samples exhibited crack growth perpendicular to the straining directions and some of the samples exhibited the formation of buckles in direction due to lateral strain.

9at.% Ag

Figure 37 shows that after annealing treatment delamination of the film is happening.

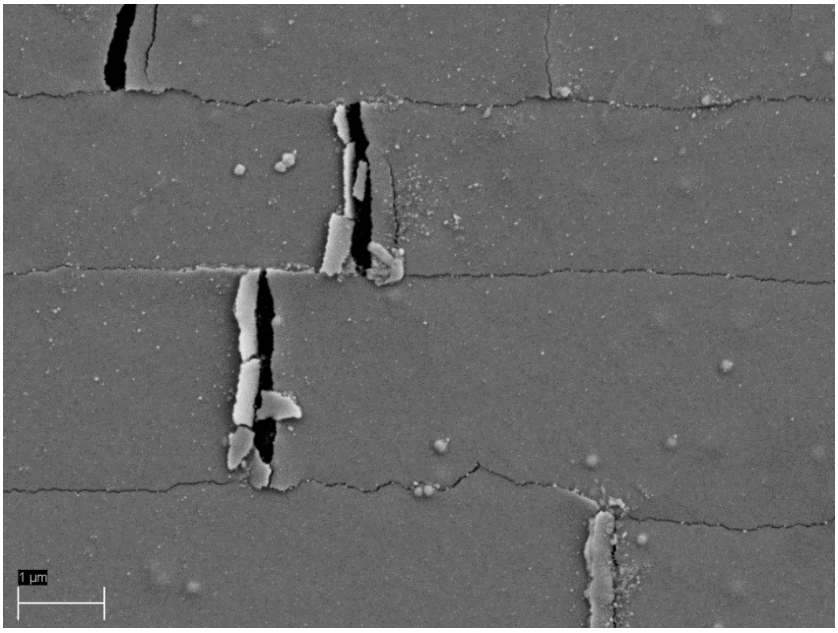

Figure 37: 9 at. % Ag after straining and annealing

18 at. % Ag

18 at.% Ag shows less delamination than 9 at.% Ag. One can see in Figure 38 that particles are built on the surface after the annealing treatment

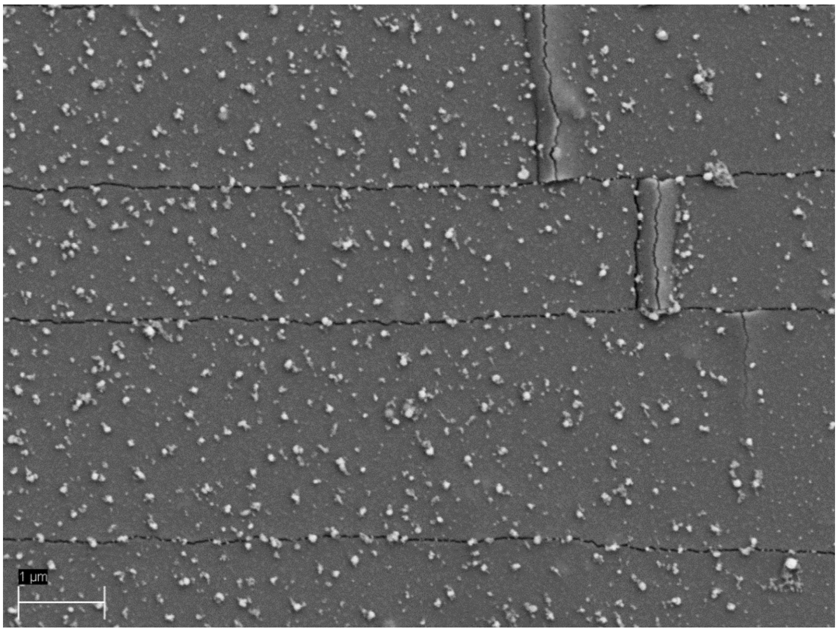

Figure 38: 18 at.% Ag after straining and annealing

25 at.% Ag

In Figure 39 the density of particles on the surface seems to increase after the heat treatment. Note that in even as deposited films of this composition have a small amount of Ag-rich particles on their surface.

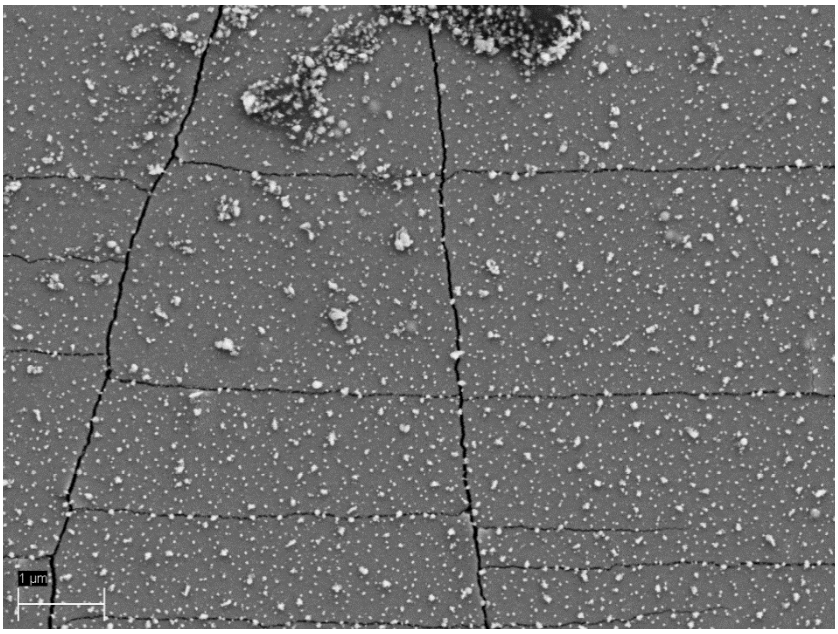

Figure 39: 25 at.% Ag after straining and annealing

31 at.% Ag

31 at.% Ag also shows particles before annealing and while annealing the particle grew. The particle film seems not to be perfect bonded to the surface since particle free paths are found and on the end of them generally bigger particle “flakes“ are found which seem to include all the particles of the particle free path (see Figure 40). This is most likely due to sample handling. Note that in contrast to the former compositions no buckles are found on the film which can be attributed to better interface adhesion with increasing Ag content.

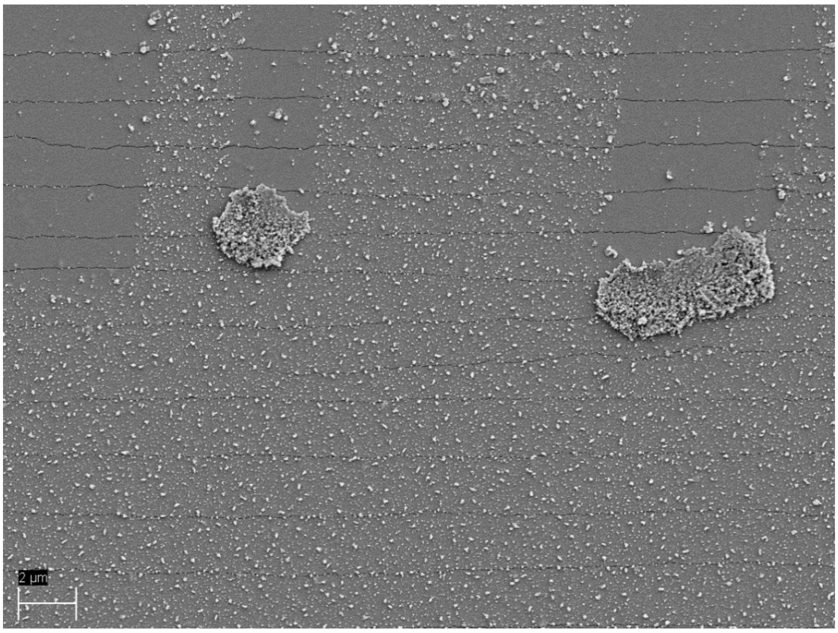

Figure 40: 31 at.% Ag after straining and annealing note that the micron bar differs to all other pictures in this chapter

44 at.% Ag

For 44at.% Ag again no buckles are obtainable and additionally the cracks seem not to go through the whole picture, as also seen on the top left of Figure 41. The particles are obvious both before and after annealing and they seem to vary in terms of shape and size. This means that even at room temperature aging happens and causes the Ag to come out of the surface.

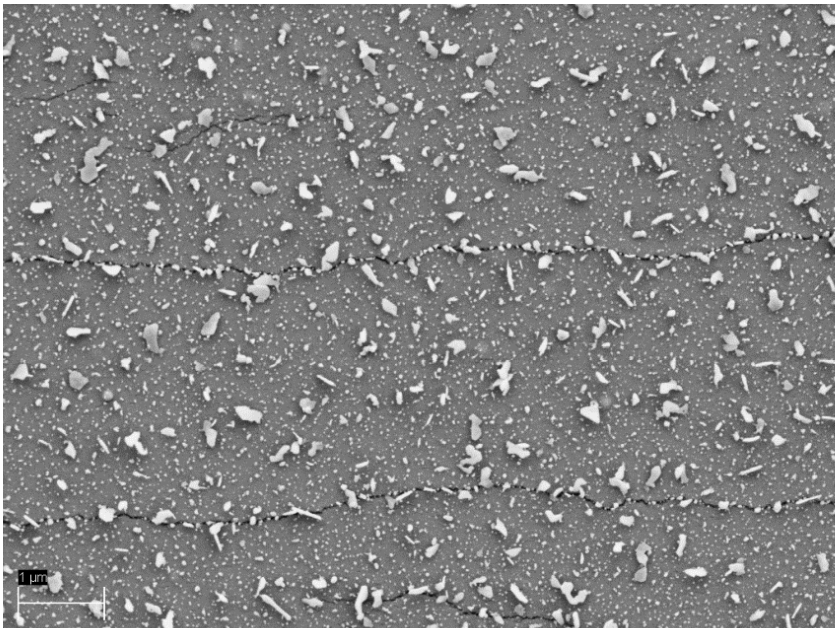

Figure 41: 44 at. % Ag after straining and annealing

100 at% Ag

In the pure silver film (Figure 42) neither cracks nor buckles were found, which indicates elastic behaviour. After annealing the film partially shows indications of delamination. Also the overall grain size seems to have been increased during the annealing treatment.

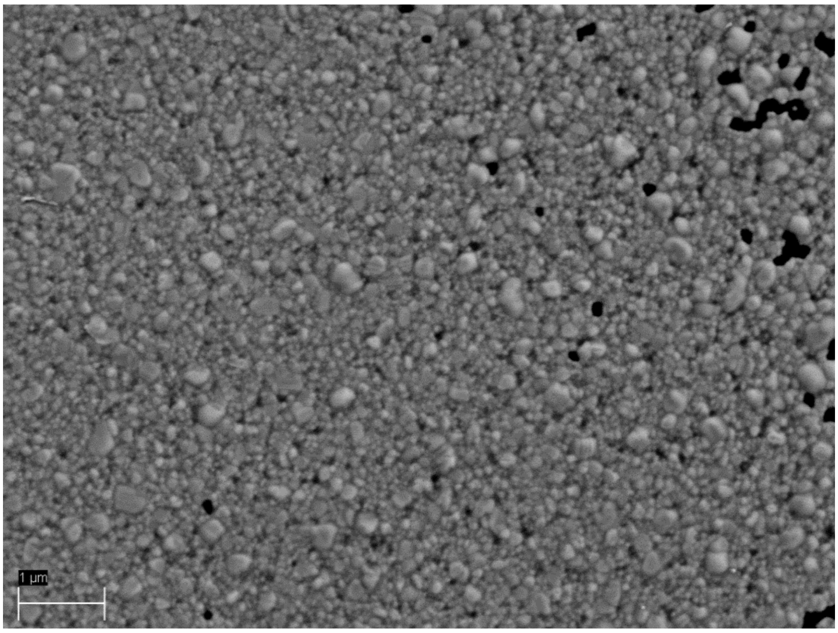

Figure 42: pure Ag after straining and annealing

5 Discussion

The presented results in the previous Chapter show that the thermo-mechanical behaviour of the Mo-Ag system are dependent in terms of changes in surface structure and segregation on rigid substrate is comparable to the behaviour of the same system on flexible substrate.

By applying the rules for sputtered binary alloy films, proposed by [17], discussed in the Literature section, one can see that the deposited films should be a polycrystalline structure. The calculated grain sizes are in agreement with theory (see Table 6 and Table 7) and suggest a nanocrystalline structure. Nanocrystalline structure was also found for electron beam evaporated Mo-Ag coatings in literature [60]. The reason for the polycrystalline structure is that the Mo-Ag system does not form any intermetallic compounds, it is immiscible (see Figure 43) and according to [12] generally like all noble metals and 5- and 6-group transition metals (V, NB, Ta, Cr, Mo and W) it shows a positive mixing enthalpy [12]. The mixing enthalpies of the Mo-Ag system can be calculated according to [12] using:

$$\Delta H(x) = E(Ag_{1-x}Mo_x) - xE(bcc - Mo) - (1-x)E(fcc - Ag) \qquad (5.1)$$

where $E(Ag_{1-x}Mo_x)$ represents the energy of the metastable solid solution (either being fcc or bcc), $E(bcc - Mo)$ and $E(fcc - Ag)$ are the energies of the equilibrium bcc-Mo/fcc-Ag phases. By using formula (5.1) it was shown by [12] that the mixing enthalpies are positive over all compositions for both crystal structures.

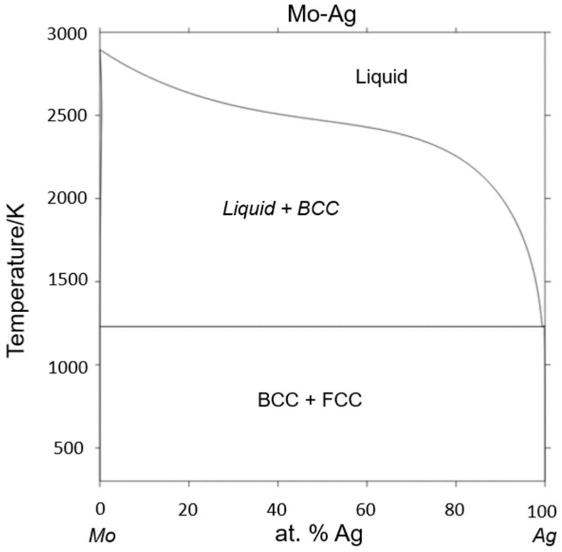

Figure 43: Calculated Ag-Mo phase diagram analogous to [61] calculated with [62]. One can see that Mo and Ag are immiscible and do not form intermetallic compounds.

The synchrotron data of Figure 16 suggests that a metastable solid solution is formed on the as deposited samples until about 44 at.% since the broadening of the peak due to Ag reaches the angle of Ag (111) at about 52 at.% Ag in 59 at. % Ag even a slight silver peak is obtained. This was also confirmed by [12], who found out by using the combined theoretical and experimental data, that films until ≤ ~46% form a bcc Mo-Ag metastable solid solution [12]. When looking at Figure 23 one can see that due to the heat treatments distinct silver peaks are measurable and the peaks generally become sharper, this means that the film segregated in a Mo-rich and an Ag-rich phases. This starts in System A at 31 at.% Ag, until then the metastable Mo-Ag solid solution is found to be more or less stable even after annealing. When comparing it to the flexible System C of the same thickness one can see that in Figure 34 the separation starts at 44 at. %Ag. This is a result of the different heat treatments of the two Systems. System A 31 at.% to 52 at.% Ag exhibited an additional annealing up to 400°C as described in Table 4. This extra time and higher Temperature enables higher diffusion rates, leading to segregation of the components at lower at.% Ag. Segregation of Ag was also seen in literature and showed that there is a thermodynamic driving force that leads to the decomposition of Mo- rich bcc alloys [12]. It results in isostructural Mo-rich and Ag-rich domains [12].

Thermal stress evolution of System B in Figure 19 is starting to change with 44 at.% Ag where the phase separation in this System should happen. The whole stress-temperature curves shift to lower stress and exhibit a higher difference in terms of stress difference between the beginning and the end of the wafer curvature experiment. Also the overall shape of the curve shifts from nearly complete elastic behaviour to pronounced non-elastic effects with increasing at.% Ag. The effect of enabling more plastic deformation with increasing amount of Ag was also found in the flexible System C. Here the crack patterns of the films after straining to 12% elongation change. The cracks become less straight and buckling due to lateral strain begins do disappear starting from 31 at.% Ag. Both changes are indications for plastic behaviour. This means that the for Mo characteristic brittle behaviour shifts to more plastic behaviour with increasing amount of silver. Pure silver films showed no signs of brittle behaviour at all. Neither cracks nor buckles formed in this system.

When looking at the *dσ/dT* slopes of both cooling and heating of System B in Table 5 one can see that the values become more negative until 25 at.% Ag and either decrease afterwards for heating or plateau more or less for cooling. This is a direct result of the metastable solid solution, it changes the interatomic potentials and directly influences the elastic modulus and the coefficient of thermal expansion. When comparing the slopes to the theoretical values, calculated in chapter 2.3.2, one can see that the effects are large.

Looking at the stress of both System A and B after annealing in Figure 20 one can see that the stress is increasing until 31 at.% Ag and decreases starting at about the end of the metastable solid solution at 44 .at% Ag. After the additional annealing of System A to 400°C as described by Figure 21 one can see that 31 at.% Ag shows less stress relief than the two systems with more Ag. This can be attributed to the increased segregation in the two other systems seen both in the θ-2θ scan of Figure 23 and the surface segregations in Chapters 4.1.2 and 4.2.3 leading to stress relief. The trend of increasing until 31 at.% Ag and decreasing afterwards was also found by the synchrotron data of System A and System C see Figure 22 and Figure 36. Generally the thicker films on Silicon (System B) always exhibited higher stresses than System A both before and after annealing, but also followed the same trend (see Figure 20). Due to the different substrate System C on Polyimide showed compressive behaviour all across the measured composition, but as described the overall same trend was measured.

The surface evolution of the rigid System B indicates slight segregations at the surface starting as low as 9at.% Ag after annealing, the flexible System C shows Ag segregation at the surface starting with 18 at.% Ag after annealing. Both evolutions become more pronounced with increasing at.% Ag. Starting with 25 at.% Ag silver particles are even obvious in System C before the annealing treatment. By comparing System B with the additionally annealed System A films one can see that the particles seem to prefer to rounder shape and tend to get bigger during the heat treatment. This can be attributed to the surface energy of the particle being minimised. Similar silver particles as described were also observed by [9–11] who experimented on yttria-stabilized zirconia (YSZ)-Mo-Ag coatings [11]. The segregation can be attributed to the high diffusion coefficient and high mobility of noble metals at elevated temperatures, leading to diffusion out of highly strained sites (surface and edges) to open surfaces resulting in a reduction of system potential and Ag grain nucleation and growth driven by surface energies [11]. The formation of silver in this thesis can be described in the same way and the weak bonding of the silver which leads to “flakes” as described in Figure 40 show that the system Mo-Ag also shows a silver film which might could be used to enhance tribological performance as described by [9–11].

Recapitulating this chapter one can say, that the wafer curvature system on rigid substrate enabled the author to estimate trends for the films on flexible substrate in terms of stress, plastic behaviour and microstructural changes.

6 Conclusions and Outlook

Thin films of Molybdenum and Silver with different compositions was sputtered on Silicon and Polyimide substrates. A wafer curvature system was used to obtain information about the film stress during different annealing treatments and to gain information about trends in terms of stress and elastic/plastic behaviour of the film. It was shown that the stresses collected with the WC system showed the same trend as the synchrotron data (evaluated with the $\sin^2\psi$ method) for both rigid and flexible substrate. Additionally, the stress-temperature curves enabled predictions of the thermo-mechanical behaviour of the flexible films. Films with pronounced non-elastic behaviour in the WC-experiments also showed crack patterns attributed to plastic deformation after straining, whereas systems that showed elastic behaviour in the WC showed brittle behaviour while straining. It was also presented that both the films on rigid as well as on flexible substrate had a nanocrystalline structure and a metastable Mo-Ag phase until about 44 at.% Ag. Segregation happened after annealing starting from compositions of about 31 at.% Ag, depending on the duration and temperature of the heating treatment. This changes were tracked using θ-2θ scan obtained with synchrotron radiation and by using SEM pictures to obtain information about the surface evolution. The surface evolution showed that segregated silver-rich particles formed on the surface and the density of particles increased with increasing amount of Silver.

This work suggests that using wafer curvature annealing experiments one can quickly estimate sufficient systems for usage in flexible microelectronics. The immiscible Mo-Ag film system should be further investigated. If the segregation process could be controlled in a way that cracks are healed it would enable usage of the system not only for tribological purposes but also in the future of longer lasting flexible microelectronics.

7 Acknowledgements

First of all I want to thank my supervisor Dr. Megan Cordill for her support, guidance, the fast corrections and the opportunity to work at BESSY II synchrotron as a student. Also thanks to everybody of her work group for support namely: Dr. Barbara Putz, Dr. Andreas Kleinbichler, Dipl. Ing. Patrice Kreiml and Dr. Oleksandr Glushko. I also want to thank Dr. Tanja Jörg very much for the deposition of the films, the pre-straining and for the bits of XRD Data I was allowed to use in this thesis.

A special thanks to Dominik Nöger BSc. for helping me with his excellent programming skills, to Dr. Thomas Schöberl for helping with the temperature correction of the wafer curvature system and to our beamline scientist Dr. Daniel Többens for helping us in the stressful time at BESSY II synchrotron.

I am very grateful to all of my colleagues, friends and comrades for discussions, chats and adventures we had during the period of writing this thesis.

I want to thank the Republic of Austria for giving every citizen the chance to get an academic education for free.

I also want to thank my parents and my family, for giving me all the opportunities and support I needed to achieve what I worked for. Finally I want to thank Vici for all the patience and support during the time of writing this thesis.

List of figures

Figure 1: Schematic of a sputter process. The plasma consists of positively charged Ions and electrons. By applying negative charge to the target, the Ions begin to impinge on it and thereby causing neutral metal atoms to be ejected. The neutral metal atoms can move through the plasma and begin to form a metallic film on the substrate. 9
Figure 2: Schematic of a double slit-experiment showing Huygens-Fresnel principle and the production of a simple diffraction pattern. The yellow areas symbolize maxima and the black areas minima of the pattern. 10
Figure 3: Schematic of ideal Debye Scherrer rings for a base centred cubic system (bcc). The corresponding crystallographic planes and angles are indicated. 11
Figure 4: Significant parts of a θ-2θ scan of sputtered Mo-Ag on Polyimide with a thickness of 50 nm. The first small peak belongs to the Ag (111) plane, the second one to Mo (110) and the last one to Mo (222). 12
Figure 5: Schematic of two different synchrotron facilities. Smileys represent electrons and outgoing SR waves. a) An older synchrotron where the radiation is only generated by bending magnets through the circular motion of the electrons. b) A modern synchrotron consisting of a particle accelerator in the middle and a storage ring around it that mainly consists of straight sections which contain insertion devices like wigglers and undulators to produce SR. Figure analogous to [28]. 13
Figure 6: Schematics of different methods to produce SR. a) Bending magnet produces SR as a result of the circular motion of the electrons. b) Wiggler works like bending magnets, but has a higher magnetic field and therefore photons with higher energies are produced. c) Undulator produces highly peaked spectrum by a small source with shallow bends. Figure analogous to [29]. 13
Figure 7: Schematic of different measurable sizes of a material (analogous to [30])....14
Figure 8: Full width at half maximum and integral breadth 15
Figure 9: Comparison Gauss and Lorentz Profiles, taken with creative common license from [40]. 17
Figure 10: Williamson and Hall plot, the crystallite size represented would be about 30.4 nm. 17
Figure 11: Schematic of Braggs law. 19
Figure 12: Shifting of diffraction peaks due to applying an external load. Decreases in the interplanar distance shifts the peaks to higher *θ* angles and vice versa for increases. 19
Figure 13: By plotting the measured d over the $\sin^2\Psi$ the stress can be calculated by measuring the slope and then using equation (2.17). a) corresponds to a compressive stress and therefore a negative slope and b) to tensile stress resulting in a positive slope. 21
Figure 14: Wafer curvature setup as described in the text analogous to [48] taken from [47] with permission. 22
Figure 15: Typical thermal evolution of stress of a Mo-Ag thin film on Silicon. 23
Figure 16: θ-2θ scan of System A films in the as-deposited state. The red-dashed-lines indicate Silver peaks and the black Molybdenum. Raw data of the graph from Tanja Jörg. 28

Figure 17: Detail of Figure 16 .The red-dashed-lines indicate Silver peaks and the black Molybdenum.......29
Figure 18: Thermal stress evolution of System A and B. Stars indicate the start of the cycle.......30
Figure 19: Overview over all compositions of System B the trends after annealing are described by Figure 20, the evolution of the thermo-elastic lines is described in Table 5 31
Figure 20: Stress before and after annealing treatment of 1h to 320°C for System A and System B.......33
Figure 21: System A Stress evolution after annealing treatment for 320°C and additional 400°C.......33
Figure 22: Film stress evolution of System A. After annealing treatments as described by Table 4. 34
Figure 23: *θ-2θ* scan of System A annealed. All compositions were annealed to 320°C for 1h and 31 to 52 at.% Ag where additionally annealed up to 400°C for 1h to enhance segregation and microstructural evolution, for details see Table 4. The red-dashed-lines indicate Silver peaks and the black Molybdenum. 35
Figure 24: 9 at.% Ag of System B after annealing to 320°C for 1h.......36
Figure 25:18 at.% Ag of System B after annealing to 320°C for 1h.......36
Figure 26: 25 at.% Ag of System B after annealing to 320°C for 1h.......37
Figure 27: 31at.% Ag of System B after annealing to 320°C for 1h.......37
Figure 28: System A 31 at% after the additional annealing to 400°C 1h.......38
Figure 29: 44 at.% Ag of System B as deposited.......38
Figure 30: 44at.% Ag of System B after annealing to 320°C for 1h.......39
Figure 31:System A 44 at.% Ag after the additional annealing up to 400°C 1h.......39
Figure 32:52 at.% Ag of System B after annealing to 320°C for 1h.......40
Figure 33:System A 52 at.% Ag after additional annealing to 400°C for 1h 40
Figure 34: *θ-2θ* of System C after straining to 15% and annealing to 350°C for 2h as described by Table 4. The red-point-dashed-lines indicate Silver peaks and the black Molybdenum.......41
Figure 35: Williamson-Hall Plot of System C for Molybdenum peaks. Every dot represents one peak as described by Figure 34. 42
Figure 36: Evolution of film stress in System C for strained and then annealed samples. Calculated using the $\mathrm{Sin}^2\Psi$-Method on the (100) peaks of Molybdenum 43
Figure 37: 9 at. % Ag after straining and annealing 44
Figure 38: 18 at.% Ag after straining and annealing 45
Figure 39: 25 at.% Ag after straining and annealing 45
Figure 40: 31 at.% Ag after straining and annealing note that the micron bar differs to all other pictures in this chapter.......46
Figure 41: 44 at. % Ag after straining and annealing 47
Figure 42: pure Ag after straining and annealing 47
Figure 43: Calculated Ag-Mo phase diagram analogous to [61] calculated with [62]. One can see that Mo and Ag are immiscible and do not form intermetallic compounds. 48

List of tables

Table 1: System A thin films on Silicon..24
Table 2: System B thicker films on Silicon..25
Table 3: System C films on Polyimide 25
Table 4: Sample overview. WC = Wafer curvature. All heating rates were 10 K/min. Slipped means the sample wasn't fixed properly in the straining device, leading to slipping during the tensile testing. Broken means sample broke before reaching 12% strain. 27
Table 5: *dσ/dT* for heating of System C in the regime of 35°C-55°C and *dσ/dT* for cooling of System C in the regime of 320°C-300°C, RMSE means Root Means Squared Error of the fit 32
Table 6: Crystallite size of Mo determined by different calculation methods for strained and annealed System C. The instrumental broadening is taken account of. For the Williamson and Hall Method the Instrumental Broadening Lorenz shape of the peak is assumed. Scherrer constant is assumed as 0.9. 42
Table 7: Crystallite size of Ag for strained and annealed System C. The instrumental broadening is taken account of. Scherrer constant is assumed as 0.9. Note that for 44 at. % Ag only one Peak was obtainable (see Figure 34 for detail). 43

References

[1] T. Jörg *et al.,* “The electro-mechanical behavior of sputter-deposited Mo thin films on flexible substrates,” *Thin Solid Films*, vol. 606, pp. 45–50, 2016.

[2] G. P. Crawford, “Flexible Flat Panel Display Technology,” in *Wiley SID series in display technology, Flexible flat panel displays*, G. P. Crawford, Ed., Chichester, West Sussex, England, Hoboken, NJ: John Wiley & Sons, 2005, pp. 1–9.

[3] W. S. Wong, Ed., *Flexible Electronics: Materials and Applications*. Boston, MA: Springer-Verlag US, 2009.

[4] T. Jörg *et al.,* “Deformation behavior of Re alloyed Mo thin films on flexible substrates: In situ fragmentation analysis supported by first-principles calculations,” *Scientific Reports*, vol. 7, no. 1, p. 7374, 2017.

[5] V. M. Marx *et al.,* “The influence of a brittle Cr interlayer on the deformation behavior of thin Cu films on flexible substrates: Experiment and model,” (eng), *Acta materialia*, vol. 89, pp. 278–289, 2015.

[6] K. D. Harris, A. L. Elias, and H.-J. Chung, “Flexible electronics under strain: A review of mechanical characterization and durability enhancement strategies,” *J Mater Sci*, vol. 51, no. 6, pp. 2771–2805, 2016.

[7] N. Demirci Sankir *et al., Molybdenum Thin Films for High Temperature Photovoltaic Fabrication Process*.

[8] A. Bollero, M. Andrés, C. García, J. d. Abajo, and M. T. Gutiérrez, “Morphological, electrical and optical properties of sputtered Mo thin films on flexible substrates,” *phys. stat. sol. (a)*, vol. 206, no. 3, pp. 540–546, 2009.

[9] C. Muratore, J. J. Hu, and A. A. Voevodin, “Adaptive nanocomposite coatings with a titanium nitride diffusion barrier mask for high-temperature tribological applications,” *Thin Solid Films*, vol. 515, no. 7-8, pp. 3638–3643, 2007.

[10] C. Muratore, A. A. Voevodin, J. J. Hu, J. G. Jones, and J. S. Zabinski, “Growth and characterization of nanocomposite yttria-stabilized zirconia with Ag and Mo,” *Surface and Coatings Technology*, vol. 200, no. 5-6, pp. 1549–1554, 2005.

[11] J. J. Hu, C. Muratore, and A. A. Voevodin, “Silver diffusion and high-temperature lubrication mechanisms of YSZ–Ag–Mo based nanocomposite coatings,” *Composites Science and Technology*, vol. 67, no. 3-4, pp. 336–347, 2007.

[12] K. Sarakinos *et al.,* “Theoretical and experimental study of metastable solid solutions and phase stability within the immiscible Ag-Mo binary system,” *Journal of Applied Physics*, vol. 119, no. 9, p. 95303, https://aip.scitation.org/doi/pdf/10.1063/1.4942840, 2016.

[13] M. Ohring, *The materials science of thin films,* 2nd ed. Boston, Mass.: Academic Press, 1993.

[14] Christian Mitterer, “Funktionswerkstoffe,” Leoben, Austria, Apr. 28 2015.

[15] Barbara Putz, “The influence of high current densities on intact and cracked thin gold films on flexible polyimide substrate,” Diploma Thesis, Erich Schmid Institute of Material Science, Montanuniversität Leoben, Leoben, Austria, 2014.

[16] E. Alfonso, J. Olaya, and G. Cubillos, *Thin Film Growth Through Sputtering Technique and Its Applications*, 2012.

[17] J. Musil and J. Vlček, “Magnetron sputtering of alloy and alloy-based films,” *Thin Solid Films*, vol. 343-344, pp. 47–50, 1999.

[18] J. Musil and F. Regent, “Formation of nanocrystalline NiCr–N films by reactive dc magnetron sputtering,” *Journal of Vacuum Science & Technology A*, vol. 16, no. 6, pp. 3301–3304, 1998.

[19] J. Musil, “Recent advances in magnetron sputtering technology,” *Surface and Coatings Technology*, vol. 100-101, pp. 280–286, 1998.

[20] J. Musil and P. Zeman, “Structure and microhardness of magnetron sputtered ZrCu and ZrCu-N films,” *Vacuum*, vol. 52, no. 3, pp. 269–275, 1999.

[21] K. Kopitzki and P. Herzog, *Einführung in die Festkörperphysik,* 6th ed. Wiesbaden: B.G. Teubner GmbH Wiesbaden, 2007.

[22] V. K. Pecharsky and P. Y. Zavalij, *Fundamentals of Powder Diffraction and Structural Characterization of Materials*. Boston, MA: Springer Science+Business Media Inc, 2005.

[23] C. Kittel, *Einführung in die Festkörperphysik,* 14th ed. München: Oldenbourg, 2006.

[24] Scott A Speakmann, *Estimating Crystallite SizeUsing XRD.* [Online] Available: http://prism.mit.edu/XRAY/oldsite/CrystalSizeAnalysis.pdf. Accessed on: Jul. 20 2018.

[25] J.'i. Mizuki, “Introduction: From a First-Generation Synchrotron Radiation to an X-ray Free Electron Laser,” *J. Phys. Soc. Jpn.*, vol. 82, no. 2, p. 21001, 2013.

[26] Greg LeBlanc, *The synchrotron light source.* [Online] Available: http://www.synchrotron.org.au/images/SynchrotronScience/machine-fact-sheet_23oct08_final.pdf. Accessed on: Jul. 23 2018.

[27] Arthur L. Robinson, “X-Ray Data Booklet: Section 2.2 HISTORY of SYNCHROTRON RADIATION,” *X-Ray Data Booklet*, 2.21-2.30, http://xdb.lbl.gov/xdb-new.pdf, 2009.

[28] David Attwood, *Synchrotron Radiation for Materials Science Applications: Intro to Synchrotron Radiation, Bending Magnet Radiation.* [Online] Available: https://people.eecs.berkeley.edu/~attwood/srms/2007/Lec08.pdf.

[29] Deutsches Elektronen-Synchrotron DESY, *SR and FEL Basics: Principles and Theoretical Background.* [Online] Available: http://photon-science.desy.de/research/students__teaching/sr_and_fel_basics/index_eng.html. Accessed on: Jul. 23 2018.

[30] Frank Girgsdies, *Peak Profile Analysis in X-ray Powder Diffraction.* [Online] Available: http://www.fhi-berlin.mpg.de/acnew/department/pages/teaching/pages/teaching__wintersemester__2015_2016/frank_girgsdies__peak_profile_fitting_in_xrd__151106.pdf. Accessed on: Jul. 20 2018.

[31] G. Gottstein, *Materialwissenschaft und Werkstofftechnik: Physikalische Grundlagen,* 4th ed. Berlin: Springer Vieweg, 2014.

[32] P. Scherrer, “Bestimmung der Größe und der inneren Struktur von Kolloidteilchen mittels Röntgenstrahlen,” Nachrichten von der Gesellschaft der Wissenschaften zu Göttingen, Mathematisch-Physikalische Klasse, Göttingen, 1918.

[33] Markus Mildner, “Komplexe Röntgendiffraktometrie an Dünnschichtsystemen,” Diplomarbeit, Fakultät Naturwissenschaften, Professur Röntgen- und Neutronendiffraktometrie, Technische Universität Chemnitz, Chemnitz, 2005.

[34] J. I. Langford and A. J. C. Wilson, “Scherrer after sixty years: A survey and some new results in the determination of crystallite size,” *J Appl Crystallogr*, vol. 11, no. 2, pp. 102–113, 1978.

[35] G.K. Williamson and W.H. Hall, “X-ray line broadening from filed aluminium and wolfram,” *Acta Metallurgica*, vol. 1, no. 1, pp. 22–31, 1953.

[36] Y. T. Prabhu, K. V. Rao, V. S. S. Kumar, and B. S. Kumari, “X-Ray Analysis by Williamson-Hall and Size-Strain Plot Methods of ZnO Nanoparticles with Fuel Variation,” *World Journal of Nano Science and Engineering*, vol. 04, no. 01, pp. 21–28, 2014.

[37] Paul Barnes, Simon Jacques, Martin Vickers, *Determination of Size and Strain: Williamson-Hall Plot.* [Online] Available: http://pd.chem.ucl.ac.uk/pdnn/peaks/sizedet.htm. Accessed on: Jul. 22 2018.

[38] M. Leoni, P. Scardi, and J. I. Langford, “Characterization of standard reference materials for obtaining instrumental line profiles,” *Powder Diffr.*, vol. 13, no. 04, pp. 210–215, 1998.

[39] C. Suryanarayana and M. G. Norton, *X-Ray Diffraction*. Boston, MA: Springer US, 1998.

[40] *Vergleich Gauß- mit Lorentzprofil.* [Online] Available: http://www.semibyte.de/wp/graphicslibrary/gl-physics/vergleich-gauss-mit-lorenzprofil/. Accessed on: Jul. 25 2018.

[41] Walther Heinz, “Mikrostrukturelle Analyse von thermomechanisch verformten und ermüdeten Al Schichten,” Dissertation, Erich Schmid Institut

für Materialwissenschaften der Österreichischen Akademie der Wissenschaften, Montanuniversität Leoben, Leoben, Austria, 2010.

[42] Fitzpatrick *et al., Determination of residual stresses by X-ray diffraction.* [Online] Available: http://www.npl.co.uk/upload/pdf/Determination_of_Residual_Stresses_by_X-ray_Diffraction_-_Issue_2.pdf. Accessed on: Jul. 16 2018.

[43] W. H. Bragg and W. L. Bragg, “The Reflection of X-rays by Crystals,” *Proceedings of the Royal Society A: Mathematical, Physical and Engineering Sciences*, vol. 88, no. 605, pp. 428–438, 1913.

[44] Peter Staron, “Einführung in die Nutzung von Streumethonden in der Werkstoffforschung: Vorlesungsskript,” Leoben, Austria, May 2018.

[45] G. G. Stoney, “The Tension of Metallic Films Deposited by Electrolysis,” *Proceedings of the Royal Society A: Mathematical, Physical and Engineering Sciences*, vol. 82, no. 553, pp. 172–175, 1909.

[46] V. Weihnacht, “Besonderheiten der mechanischen Eigenschaften und der Mikrostruktur dünner, polykristalliner Kupferschichten,” Dissertation, Fakultät für Werkstoffwissenschaft und Werkstofftechnologie, Technischen Universität Bergakademie Freiberg, Freiberg, 2001.

[47] Claus O. W. Trost, “Influence of the film thickness on the thermo-mechanical properties of different copper metallizations,” Bachelor Thesis, Department Materials Physics, Montanuniversität Leoben, Leoben, Austria, 2017.

[48] E. Chason, “Resolution and sensitivity of stress measurements with the k-Space Multi-beam Optical Sensor (MOS) System,” Sandia National Laboratories, 2005.

[49] S. Bigl, S. Wurster, M. J. Cordill, and D. Kiener, “Advanced characterisation of thermo-mechanical fatigue mechanisms of different copper film systems for wafer metallizations,” *Thin Solid Films*, vol. 612, pp. 153–164, 2016.

[50] P. A. Flinn, D. S. Gardner, and W. D. Nix, “Measurement and Interpretation of stress in aluminum-based metallization as a function of thermal history,” *IEEE Trans. Electron Devices*, vol. 34, no. 3, pp. 689–699, 1987.

[51] C. A. Swenson, “Recommended Values for the Thermal Expansivity of Silicon from 0 to 1000 K,” *Journal of Physical and Chemical Reference Data*, vol. 12, no. 2, pp. 179–182, 1983.

[52] Plansee, *Molybdenum | Plansee.* [Online] Available: https://www.plansee.com/en/materials/molybdenum.html. Accessed on: Aug. 07 2018.

[53] W. D. Callister, *Materials science and engineering: An introduction,* 5th ed. New York: Wiley, 2000.

[54] D. Mende and G. Simon, *Physik: Gleichungen und Tabellen*: Carl Hanser Verlag GmbH & Company KG, 2016.

[55] S. Bigl, C. O.W. Trost, S. Wurster, M. J. Cordill, and D. Kiener, “Film thickness dependent microstructural changes of thick copper metallizations upon thermal fatigue,” *J. Mater. Res.*, vol. 32, no. 11, pp. 2022–2034, 2017.

[56] Helmholz-Zentrum Berlin, *KMC2-diffractometry: (version 2006_09_10).* [Online] Available: https://www.helmholtz-berlin.de/pubbin/igama_output?modus=datei&did=284. Accessed on: Jul. 27 2018.

[57] D. M. Többens and S. Zander, “KMC-2: An X-ray beamline with dedicated diffraction and XAS endstations at BESSY II,” *JLSRF*, vol. 2, 2016.

[58] J. C. Slater, “Atomic Radii in Crystals,” *The Journal of Chemical Physics*, vol. 41, no. 10, pp. 3199–3204, 1964.

[59] T. L. Smith and C. S. Kim, “Thermal Expansion And Viscoelastic Properties Of A Semi-Rigid Polyimide,” *MRS Proc.*, vol. 227, 1991.

[60] R. Chattopadhyay, *Advanced Thermally Assisted Surface Engineering Processes*: Springer US, 2007.

[61] *Calculated Ag-Mo phase diagram.* [Online] Available: http://resource.npl.co.uk/mtdata/phdiagrams/agmo.htm. Accessed on: Aug. 20 2018.

[62] Davies, R H, Dinsdale, A T, Gisby, J A, Robinson, J A J, Martin, S M, “MTDATA - thermodynamic and phase equilibrium software from the National Physical Laboratory.,” in *CALPHAD Comput. Coupling Phase Diagr. Thermochem.*, pp. 229–271.